Imaging of PARP1/2-Overexpressing Cancers with Novel AZD2281-Derived Probes

Citation

Permanent link

Terms of Use

Share Your Story

Table of Contents

Abstract

For this project, targeted imaging of pancreatic and ovarian cancers with inhibitor-derived probes was investigated. Fluorescent and radioactive derivatives of AZD2281, a poly(ADP-ribose)polymerase-1 and -2 (PARP1/2) inhibitor, were screened in a panel of pancreatic and ovarian cancer cell lines found to overexpress PARP1/2. We hypothesized that the AZD2281-derived probes would serve as accurate measures of PARP1/2 expression and inhibition.

To test this hypothesis, a panel of pancreatic ductal adenocarcinoma and ovarian carcinoma cell lines were characterized by Western blot and immunocytochemistry for PARP1/2 expression. Cells were then treated with AZD2281-BODIPY FL, fixed, and stained with anti-PARP. Fluorescence at 515 nm (AZD2281-BODIPY FL) correlated with fluorescence at 670 nm (anti-PARP), indicating that PARP1/2 expression level is associated with fluorescent signal strength of AZD2281-BODIPY FL *in vitro*.

Four cell lines representing a range of PARP1/2 expression were xenografted into Nu/Nu mice and the tumors grown. Mice bearing four tumor types each were imaged with AZD2281-BODIPY FL or ^{18}F-AZD2281, sacrificed, and their tumors excised for stand-alone imaging and Western blot. Tumor fluorescence at 515 nm and standardized uptake values (SUVs) from PET-CT correlated with tumor PARP1/2 expression measured by Western blot, indicating that PARP1/2 expression level is a determinant of fluorescent and radioactive signal strength of AZD2281-based imaging agents *in vivo*. Significantly more AZD2281-BODIPY FL and ^{18}F-AZD2281 accumulated in tumors than in control muscle, providing clear visualization of PARP1/2-overexpressing cells *in vivo*.

Finally, ^{18}F-AZD2281 and ^{18}F-fluorodeoxyglucose (FDG), the currently favored imaging probe for PET-CT oncology studies, were compared in a cohort of mice bearing A2780 tumors in their flanks. Mice were subjected to PET-CT to obtain baseline SUVs for both ^{18}F-AZD2281 and ^{18}F-FDG. Over the following three days, mice were given doses of unmodified AZD2281 drug and imaged with PET-CT in triplicate. While SUVs for ^{18}F-FDG were unchanged by administration of AZD2281, ^{18}F-AZD2281 SUVs were significantly reduced compared to baseline signal. These data indicate that PET-CT imaging with ^{18}F-AZD2281, but not ^{18}F-FDG, can quantify PARP1/2 inhibition *in vivo*.

The most commonly performed PET study involves imaging cancers with the radiotracer fluorodeoxyglucose (^{18}F-FDG); however, glucose-avidity is not a cancer-specific trait and it varies between and within tumor types. Perhaps more importantly, changes in FDG uptake are not always predictive early markers of molecularly targeted cancer drugs, hence the need for other imaging agents. The overall goal of this study was to determine whether a newly developed, drug-derived small molecule imaging agent could be used to quantitate PARP inhibition in ovarian and pancreatic cancers. Measurement of PARP inhibition may improve clinical observation of progression and treatment efficacy in patients receiving PARP inhibitors. This research represents a step toward developing a more generic approach for the rapid codevelopment of companion imaging agents based on small-molecule therapeutic inhibitors.

Acknowledgements

My thesis project would not have been possible without the support and guidance of many. First, I would like to thank Dr. Ralph Weissleder for providing me with the incredible opportunity to work in and learn from his lab. Under his watch I have grown and learned more than I had thought possible in such a short span of time.

I would also like to thank all of the brilliant and capable members of the Weissleder lab as well as the many individuals in the Health Sciences & Technology program who have helped me. I would especially like to thank Thomas Reiner for his mentorship, support, and humor, without which this work would never have been completed. You made sure I was productive and happy, and you've taught me so much. I am forever grateful.

I am also indebted to Ned Keliher for sharing his expertise and experience with me. I owe special thanks to Katy Yang, Adeeti Ullal, and Sarah Earley for their patience in teaching me the ropes of all-things-*in vitro*. Their advice was invaluable to the successful completion of this project.

I must also acknowledge the contributions of Josh Dunham, who saved the day on many occasions when microscopy went awry; Rostic Gorbatov, who introduced me to working with mice and masterfully attended to our mouse-surgery needs; and Rainer Kohler, who aided with *in vivo* imaging of window chambers.

To the entire Weissleder lab, I would like to say thank you for making me feel at home. I am honored to have been a part of such a special group of people. You have all inspired me to ask better questions and become a better scientist.

I would finally like to thank my family and friends for their love and support. With your encouragement I made it through an occasionally stressful, profoundly wonderful year.

Glossary

^{18}F	^{18}fluorine
^{18}F-FDG	fluorodeoxyglucose
ADP	adenosine diphosphate
BCA	bicinchoninic acid
CT	computed tomography
DMAC	dimethylacetamide
DMSO	dimethyl sulfoxide
DSB	double strand break
IC_{50}	half maximal inhibitory concentration
FLT	^{18}F-fluorothymidine
Gab	IgG antibody
GAPDH	glyceraldehyde 3-phosphate dehydrogenase
keV	kilo-electron volt
Mab	IgM antibody
PARP	poly(ADP-ribose) polymerase
PBS	phosphate buffered saline
PEG	polyethylene glycol
PET	positron emission tomography
PFA	paraformaldehyde
RIPA	radioimmunoprecipitation assay buffer
SSB	single strand break
SUV	standardized uptake value
TBS	tris-buffered saline

Chapter 1: Introduction

1.1 Significance

Despite decades of intense research, cancers continue to be a threatening family of diseases. Cancers are often treated with inhibitors, which may or may not work for an individual patient based on the cancer's particular genetic and metabolic properties. The complexity of managing ovarian and pancreatic cancers is a particularly demanding and challenging problem. The initial choice of chemotherapy regimen is important, as survival times are short and progression may preclude the patient from trying other agents. Functional imaging of biomarkers may allow for better understanding of cancers at the molecular level, permitting better management of these diseases.[1,2]

An estimated 22,240 women in the United States were diagnosed with ovarian cancer in 2013, and 14,030 women died of the disease.[3] Over sixty percent of ovarian cancers are diagnosed after metastasis has already occurred. While women with disease confined to regional lymph nodes have a 91.9% 5-year survival rate, women with metastatic disease have only a 27.3% survival rate at 5 years.[3] The poor survival rates may be partly explained by the high rates of recurrence, with 70% of stage III and IV patients and 20-25% of stage I and II patients relapsing after initial treatment.[4] While assays that stratify ovarian tumors into platinum chemotherapy "sensitive" and "resistant" categories have been developed, these assays do not predict the most effective regimen for a patient's cancer.[5]

Pancreatic cancer struck an estimated 45,220 Americans and killed 38,460 in 2013.[6] They have an even more dismal prognosis than ovarian cancers: 5-year survival rates for patients with

localized, regional spread, and metastatic disease are only 24.1%, 9.0%, and 2.0%, respectively.[6] The overwhelming majority of patients are diagnosed after the cancer has spread regionally (27%) or has metastasized (53%).[6] Gene profiling is currently being studied to identify patients who are sensitive or resistant to the most common chemotherapeutic regimens,[7] though standard chemotherapy regimens in advanced pancreatic cancer have low response rates with improvement in survival times only on the order of months.[8]

Functional molecular imaging (such as positron emission tomography, or PET) for screening and diagnostic purposes is controversial, but it is already playing an important role in cancer staging and is increasingly being used to monitor disease progression, recurrence,[9] and treatment efficacy.[10,11] By far the most commonly performed PET study involves imaging cancers with the radiotracer fluorodeoxyglucose (^{18}F-FDG).[12] However, glucose-avidity is not a cancer-specific trait and it varies between and within tumor types.[13] For example, many benign adnexal conditions (including endometriosis, cystadenomas, teratomas, schwannomas, and even normal ovaries in menstruating women) may strongly take up ^{18}F-FDG, while borderline or mucinous ovarian adenocarcinomas may fail to take up more ^{18}F-FDG than background structures.[14] Scanning for pancreatic cancers with ^{18}F-FDG can result in false negative results in patients with high serum glucose levels, and false positives can occur in patients with pancreatitis.[15] Indeed, PET imaging may miss tumors in any highly metabolically active[16] or inflamed[17] tissues.

Employing radiotracers that bind specific molecular targets in cancer cells may present the opportunity to detect and monitor malignancy with improved specificity. Moreover, visualizing drug targets *in vivo* could predict which tumors are likely to respond to that drug in a chemotherapeutic regimen. This predictive ability might allow for rational, individualized

treatment choice. Additionally, the increased specificity of targeted imaging may help clinicians to improve staging and monitoring of progression or development of resistance of ovarian and pancreatic cancers. For this project, I investigated a novel targeted radiotracer, discussed in section 1.4, for its potential utility in PET imaging pancreatic and ovarian cancers. This study represents one of the first attempts to measure targeted inhibition in cancers.

1.2 Positron Emission Tomography-Computed Tomography

Positron Emission Tomography-Computed Tomography (PET-CT) has emerged as an important tool, especially in oncology, where it is widely used in cancer diagnosis and staging. PET-CT has been increasingly used to monitor cancer progression and treatment efficacy. Because this project investigated a novel targeted PET radiotracer, I will first aim to provide brief overviews of PET imaging and currently available radiotracers before discussing the need for an expanded group of imaging probes.

1.2.1 Physics of PET

PET imaging requires injection with radioactive tracers that decay by emission of positrons (positively charged particles with the mass of an electron). Positrons travel short distances, losing energy via scattering interactions with electron clouds of nearby atoms, before directly encountering an electron from an atom in the surrounding matter. The range, or distance traversed by the positron, depends on the energy of the positron (which, in turn, is a function of the radionuclide that emitted the positron). The joining of positron and electron results in mutual annihilation and the release of two 511 keV photons offset approximately 180° from each other.

PET scanners contain opposing detectors that record the arrival of divergent annihilation photons if these photons arrive within a narrow time frame relative to one another. The photons are

assumed to have originated at a collision point somewhere along the straight line between the two detectors that recorded the event.

1.2.2 Combined PET-CT

PET by itself often produces unsatisfactory images. Because PET scanners detect annihilation points rather than positron emission points, there is a limit to the spatial resolution determined by the range of emitted positrons. (The most commonly used isotope, [18]fluorine or ^{18}F, produces low energy positrons that have a short range – maximum 2.4mm – that produce relatively high resolution images[18]). Additionally, the residual momentum of the positron and subsequent non-collinearity of the annihilation photons also limits the maximum spatial resolution achievable by PET alone: the assumption of collinearity by the image-processing algorithm typically mislays the coincidence line by less than 0.5°, with the effect of blurring by 1-2 mm depending on the diameter of the scanning ring.[19] Finally, attenuation limits the usefulness of standalone PET. Because photons traveling through the body may be absorbed or lose energy, fewer photons are detected than are emitted from deep regions while relatively more photons are detected from superficial structures, leading to information degradation and artifacts.

The moderately low spatial resolution of PET and the lack of a well-defined anatomical reference frame in its images quickly led to the use of integrated PET-CT scanners, which perform PET and CT imaging in tandem during a single examination. CT scanners use x-rays to acquire high-resolution anatomical images and to perform attenuation correction. The combination of an anatomical and attenuation map from CT with the positron emission map from PET enables accurate assessment of the activity of deep body structures with appropriate damping of the signal from superficial structures. For this project, we used PET-CT for all experiments with ^{18}F-labeled radioactive imaging agents.

1.2.3 Current Radiopharmaceuticals

1.2.3.1 Fluorodeoxyglucose

The isotope of choice in medical radiochemistry is ^{18}F. In addition to the relatively good spatial resolution afforded by the short range of its emitted positrons,[18] ^{18}F has a relatively long and biocompatible half-life of 110 minutes, permitting the uncoupling of its synthesis and use (for example, allowing transport to distant sites that lack access to a cyclotron). Owing to its half-life, ^{18}F is suitable for imaging studies that may last several hours, but its half-life is short enough to keep radiation exposure to the injected patient within reasonable limits.

Of all ^{18}F radiotracers devised, none is more widely used in medicine than ^{18}F-fluorodeoxyglucose (^{18}F-FDG). Ninety-percent of all PET studies are performed for oncology patients using ^{18}F-FDG.[12] The rationale for use of a glucose analog in cancer imaging stems from the increased metabolic demands of malignant proliferating cells. Glucose-avid tumors import ^{18}F-FDG through overexpression of glucose transporters (e.g. GLUT1, GLUT3) and trap ^{18}F-FDG in the cell via hexokinase-mediated phosphorylation. ^{18}F-FDG-6-phosphate cannot be assimilated into glycogen nor can it be further metabolized in glycolysis because it lacks a crucial 2'-hydroxyl group. Thus, tumor cells accumulate ^{18}F-FDG-6-phosphate to a greater extent than the surrounding normal tissue and can be visualized by PET.

However, ^{18}F-FDG has its limitations (Table 1). Certain tissues in the body, such as brain, kidney, bladder, and myocardium, normally exhibit high levels of glucose uptake. Glucose-avidity is thus not a cancer-specific trait, and it varies between and within tumor types.[13] Moreover, ^{18}F-FDG PET imaging may miss tumors in metabolically highly active[16] or inflamed[17]

tissues. Changes in ^{18}F-FDG uptake are also not always predictive early markers of effects of molecularly targeted drugs. To reduce competition from unlabeled glucose and to minimize the effects of insulin on uptake of glucose (and its analogs) at normal tissues, use of ^{18}F-FDG also requires that the patient fasts and achieves blood glucose levels below 120-150 mg/dL[17,19], which may be problematic for diabetics.

1.2.3.2 Other [18]Fluorine Radiotracers

In addition to ^{18}F-FDG, other ^{18}F radiotracers (many more than can be discussed here) have been developed for PET imaging. For example, fluoride ions can replace hydroxide ions in the bone's inorganic hydroxyapatite matrix and ^{18}F-fluoride labels regions of altered bone metabolism, exploiting the amplified local blood flow, higher capillary permeability, and increased bone turnover that is characteristic of malignant bone lesions.[20] ^{18}F-fluoride identifies the reactive bone process rather than tumor cells themselves, and is thus considered a nonspecific tracer for cancer.[18]

Other ^{18}F radiotracers have been developed that mark highly proliferative cells based on their increased rate of macromolecule synthesis. Some agents mark cells with elevated DNA synthesis rates, such as the nucleoside analogs ^{18}F-fluorothymidine (FLT), ^{18}F-fluorouridine, and 2'-[^{18}F]fluoro-5-methyl-1-β-D-arabinofuranosyluracil (^{18}F-FMAU). These agents are taken up by rapidly dividing cells, trapped via phosphorylation, and persist due to inefficient degradation. In addition to nucleic acids, rapidly dividing tumor cells are known to generate large quantities of phospholipids like lecithin and subsequently take up large amounts of choline,[21] which led to the development of the probe ^{18}F-fluoroethylcholine. Probes that identify rapid cell proliferation have the advantage of being more tumor-specific than ^{18}F-FDG.[18]

Of the radiotracers that label rapidly dividing cells, ^{18}F-FLT has been most extensively studied. Although PET quantification of ^{18}F-FLT uptake has been shown to correlate with biopsy-based proliferation scores (such as the Ki-67 score in lung, brain, lymphoma, breast, colorectal, esophageal, and head and neck cancers, melanomas, and soft tissue sarcomas of the extremities),[22] the usefulness of ^{18}F-FLT versus ^{18}F-FDG remains controversial since ^{18}F-FLT is not incorporated into DNA[18] and therefore does not definitively reflect the rate of DNA synthesis.[16,18]

Besides proliferation, other common tumor features such as hypoxia and angiogenesis have also been explored in the development of novel PET radiotracers. ^{18}F-fluoromisonidazole (FMISO), derived from the antibiotic 2-nitroimidazole that targets anaerobes, is used to image tumor hypoxia (an important prognostic factor). Upon diffusion into cells, nitroimidazoles are reduced by a single electron to generate a radical anion species. In the absence of oxygen, the nitroimidazole radical fails to be reoxidized and covalently bonds to intracellular macromolecules and labels the hypoxic cell.[23] Clinical trials (summarized by Rice et al., 2011) investigating the angiogenesis marker ^{18}F-Galacto-RGD, which binds the capillary cell integrin $\alpha_v\beta_3$, have demonstrated the ability of the probe to measure integrin expression and angiogenesis in patients.[24]

1.2.3.3 Targeted Imaging

Much of the functional molecular imaging has focused on exploiting common cancer traits across tumor types, such as altered metabolism, proliferation, hypoxia, and angiogenesis. However, the appreciation of the patient-specificity of cancers makes the ability of molecular imaging to identify specific genotypes or phenotypes with targeted probes increasingly attractive. Some of the oldest targeted radiotracers, the ^{18}F-fluoroestradiols, can actually detect estrogen

receptor positive breast tumors and may one day help non-invasively predict responsiveness to tamoxifen therapy.[25,26,18] Another example of targeted PET involves the radiotracer [124]I-cG250 derived from a chimerized monoclonal antibody against carbonic anhydrase IX, an antigen expressed by 94% of renal clear-cell carcinomas.[27] Renal carcinomas are difficult to visualize with ^{18}F-FDG due to the high physiologic uptake of the probe by the normal kidney. [124]I-cG250 permits cancer identification and stratification into aggressive ([124]I-cG250 uptake-positive) and less aggressive ([124]I-cG250 uptake-negative) phenotypes.[27] Other targeted PET radiotracers may similarly enable physicians to move beyond cancer detection towards increased sophistication in determining prognosis, selecting treatment, monitoring progression, and early identification of therapeutic resistance.

1.3 PARP in Cancers

For this project, we investigated the utility of a molecularly targeted probe against poly(ADP-ribose)polymerase (PARP), an enzyme involved in both single strand break (SSB) and double strand break (DSB) repair, in imaging ovarian and pancreatic cancers. Some ovarian and pancreatic cancers (up to 82%[28] and 10%[29], respectively) have been shown to have inherited or sporadic BRCA mutations. BRCA1 and BRCA2 are proteins involved in homologous recombination repair mechanisms that mend DNA double strand breaks (DSBs).[30] BRCA-deficient tumors rely on other DNA repair mechanisms such as those mediated by PARP to preserve genomic integrity.[31-33]

PARP1 and PARP2 are nuclear proteins that recognize sites of DNA damage and form large, branched chains of ADP-ribose on specific DNA-associated proteins, such as histones and themselves.[34-36] These poly(ADP-ribose) chains disrupt protein function and recruit potentially hundreds of proteins,[34] including XRCC1, which orchestrates base excision repair.[37] Tumors with

defects in homologous recombination pathways, including BRCA1- and BRCA2-deficient cancers, have been shown to be sensitive to inhibition of PARP1-mediated DNA repair with PARP1 inhibitors alone or in combination with DNA damaging agents (e.g. cis-[Cl$_2$Pt(NH$_3$)$_2$]).[31-33,38] BRCA-deficient tumors[31-33] or tumors with non-BRCA defects in homologous recombination[38,39] are thought to be sensitive to PARP inhibitors due to the synthetic lethality originating from the elimination of both BRCA and PARP dependent DNA repair pathways.

1.4 AZD2281-based Imaging Agents

Several PARP inhibitors are currently in clinical trials for a variety of advanced cancers,[40,41] and the Weissleder group has developed fluorescent and radioactive imaging agents based on one such competitive inhibitor, AZD2281 (Olaparib; Figure 1A).[42,43,44] The Weissleder lab has shown that the radiofluorinated PARP1 inhibitor ^{18}F-AZD2281 synthesized by our group accumulates in a BRCA-mutant breast cell line that has high PARP1 expression (MDA-MB436), enabling the use of this inhibitor as a radiotracer for PET-CT of xenografts of this cell line $in\ vivo$.[44] Although we have imaged the increased PARP1 levels for BRCA-mutant breast cell lines (MDA-MB436) versus BRCA-wild type breast cancer cell lines (MDA-MD231), not much is known about PARP1 protein levels and activities in other tumor cells and in healthy cells.[34] Moreover, the ability of the ^{18}F-AZD2281 probe to accurately quantify varying levels of its PARP target had not been previously demonstrated. I investigated the relative levels of PARP1/2 in cancerous cells lines and healthy tissue to determine if the scope of AZD2281-derived imaging agents can be widened to different forms of cancer, specifically pancreatic ductal adenocarcinomas and ovarian cancers. We hypothesized that AZD2281-derived imaging agents would serve as an accurate measure of PARP1/2 expression.

Chapter 2: Methods

All experiments described in the following methods section were carried out by myself. HT1080 H2b-apple cells were generated by Katherine S. Yang. ^{18}F-AZD2281 was synthesized by Edmund J. Keliher and Thomas Reiner. Experiments involving radiochemistry were performed in their presence.

2.1 PARP-1 IC$_{50}$ Determination

PARP-1 activity in the presence of graduated amounts of AZD2281-BODIPY FL was measured *in vitro* with a commercially available colorimetric assay (Trevigen, Gaithersburg, MD). Triplicate experiments with varying concentrations of AZD2281-BODIPY FL (3.3 μM to 0.1 nM) were performed using 0.5 units PARP high-specific activity (HSA) enzyme in histone-coated 96-well plates, each incubated for 10 minutes. Positive control wells contained no AZD2281-BODIPY FL. Negative control wells had no PARP-1. Each well contained a final volume of 50 μL with a final concentration of 2% DMSO in assay buffer. The rest of the assay was carried out according to the manufacturer's instructions. A Tecan Safire^2 microplate reader (Tecan Group, Mannedorf, Switzerland) was used to measure PARP-1 activity via absorbance at 450 nm. Calculation of IC$_{50}$ values was performed using Prism software (GraphPad, La Jolla, CA).

2.2 PARP-2 IC$_{50}$ Determination

PARP-2 activity in the presence of graduated amounts of AZD2281-BODIPY FL was measured *in vitro* with a commercially available chemiluminescence assay (BPS Biosciences, San Diego, CA). Triplicate experiments with varying concentrations of AZD2281-BODIPY FL (3.3 μM to 0.1 nM) were performed using 50 ng PARP-2 enzyme in histone-coated 96-well plates. Positive control wells contained no AZD2281-BODIPY FL. Negative control wells had no PARP-2. Each

well contained a final volume of 50 μL with a maximum final concentration of 2% DMSO in assay buffer. The rest of the assay was carried out according to the manufacturer's instructions. A Tecan Safire[2] microplate reader (Tecan Group, Mannedorf, Switzerland) was used to measure PARP-2 activity via chemiluminescence. Calculation of IC_{50} values was performed using Prism software (GraphPad, La Jolla, CA).

2.3 Cell Culture

Cell lines were obtained from Prof. Michael Birrer's lab at Massachusetts General Hospital (UCI 101, UCI 107, OVCAR429, A2780), Katy Yang in the Weissleder lab (HT1080 stably expressing H2b-apple), and the ATCC (all remaining cell lines). Cells were cultured in their respective appropriate growth media. Briefly, MDA-MB231, MDA-MB436, MIA PaCa2, A2780, OVCAR429, UCI 101, and UCI 107 cells were grown in RPMI 1640 with 10% fetal bovine serum, L-glutamine, and penicillin/streptomycin. RAW 264.7, PANC1, CaOV3, and HT1080 cells were grown in DMEM with 10% fetal bovine serum, 2% sodium bicarbonate, L-glutamine, and penicillin/streptomycin. SKOV-3 cells were grown in McCoy's 5A medium with 10% fetal bovine serum, L-glutamine, and penicillin/streptomycin. OVCAR-3 cells were grown in RPMI 1640 with 20% fetal bovine serum, 1% bovine insulin, L-glutamine, and penicillin/streptomycin. OV-90 cells were grown in 50% MCDB 105 medium, 50% Medium 199 with 15% fetal bovine serum, and 2% sodium bicarbonate. All cell lines were incubated at 37°C and 5% CO_2. Cells were harvested by trypsinization (0.25% trypsin-EDTA) for all experiments involving cells.

2.3.1 HT1080 H2b-apple

Katy Yang transformed the HT1080 cell line to stably express H2b-apple as detailed in Reiner et al 2012.[45]

2.4 *In vitro* Imaging of AZD2281-BODIPY FL

Unless otherwise noted, all *in vitro* images were captured on the Deltavision (Applied Precision Instruments) and Olympus IX71 microscopy system and fluorescence intensities were calculated using public domain ImageJ software (National Institutes of Health, Bethesda, MD).

2.4.1 Cell imaging

To determine if probe uptake occurs specifically at the molecular targets of AZD2281 (i.e. PARP1/2), AZD2281-BODIPY FL *in vitro* imaging and blocking experiments were performed. MIA PaCa2, MDA-MB231, and MDA-MB436 cells (200 μL, 50,000 cells/mL) were seeded into glycerine-treated 8-well chamber slides (Lab Tek^{TM}, Thermo Scientific, Rochester, NY), and allowed to attach over night. Cells were then incubated with AZD2281 (2 μL, 1 mM) or medium (1% DMSO) for 20 minutes (37 °C) before the medium was removed and cells were washed (1x, medium, 500 μL). Subsequently, 200 μL medium and AZD2281-BODIPY FL (2 μL, 100 μM) were added and incubated at 37 °C for 15 min. Cells were washed with PBS (1x 500 μL), fixed with paraformaldehyde (4% in PBS) and washed with PBS/0.1% Triton X-100/0.5% bovine serum albumin (3x 500 μL, 3rd wash left for 15 min), before they were incubated with anti-PARP-1 Mab (1:200; Millipore, Billerica, MA) at 4 °C over night. Cells were washed with PBS/0.1% Triton X-100 (3x 200 μL) before they were stained with secondary IgG-Cy5 Gab (1:100; Millipore, Billerica, MA) for 3h at 4 °C. Cells were then washed with PBS (1x, 200 μL), stained with Hoechst (Invitrogen, Carlsbad, CA) and blue whole cell stain (Thermo Scientific, Rochester, NY) for 30 min at room temperature, and washed with PBS (3x, 200 μL) before imaging on the Nikon 80i (60x, 1x zoom).

2.4.2 Co-localization of AZD2281-BODIPY FL and PARP1/2

To characterize the AZD2281-BODIPY FL co-localization with PARP1/2 in cells, RAW 264.7, PANC1, MIA PaCa2, A2780, OVCAR429, UCI 101, UCI 107, SKOV-3, OVCAR-3, and OV-90

cells (200 μL of 35,000 cells/mL) were plated in their appropriate growth media on 96-well plates then allowed to attach for 48 hours. The cells were then incubated with AZD2281-BODIPY FL (2 μL, 100 μM, 20 min, 37 °C). The medium was removed and cells were washed (1x, medium, 200 μL and 2x 1X PBS), fixed (4% PFA in PBS) and permeabilized (ice cold PBS/0.1% Triton X-100/0.5% bovine serum albumin for 3x 200 μL permeabilizations: 2x 5 min and then 1x 30 min). Next, anti-PARP1/2 polyclonal antibody (1:50; Santa Cruz Biotechnology, Santa Cruz, CA) was applied and incubated at 4 °C over night. Then, the cells were washed with PBS/0.1% Triton X-100 (3x 200 μL) and stained with secondary IgG-Cy5 goat antibody (1:100; Millipore, Billerica, MA) for 3h at 4 °C. Cells were washed with PBS (1x, 200 μL), stained with Hoechst 33342 (Invitrogen, Carlsbad, CA) and blue whole cell stain (Thermo Scientific, Rochester, NY) for 30 min at room temperature, and washed with PBS (3x, 200 μL) before imaging. Imaging was done on a DeltaVision microscope (Applied Precision Instruments) at 20X, with 1.6 zoom. For each cell line, 9 distinct regions were measured per well. All cell lines were measured in biological and technical triplicate. AZD2281-BODIPY FL fluorescence was measured and calculated by quantification of fluorescence signal and subtraction of green autofluorescence in the respective cell lines. PARP1/2 expression levels were measured and calculated by quantification of the fluorescence signal and subtraction of nonspecific secondary IgG-Cy5 Gab staining. Using open source image processing package Fiji for ImageJ, co-localization of anti-PARP1/2 and AZD2281-BODIPY FL fluorescence signals was quantified as a Pearson's correlation coefficient comparing intensity of each pixel in the red and green channels, respectively (R_{coloc} = 0.95).

2.4.3 Western Blot

Western blots were performed to determine PARP1/2 expression for both cultured cell line samples as well as excised tumors from sacrificed mice (see section 2.5.6). Samples were

suspended in 1x RIPA buffer and 2x Mini Complete Protease Inhibitor Cocktail tablet (Roche, Indianapolis, IN). The samples were centrifuged at 4°C, 10,000 rpm for 10 minutes and the protein-containing supernatant saved. The protein concentration of each sample was measured with a BCA Protein Assay performed according to manufacturer's instructions (Therno Scientific, Rochester, NY). 10 μg of the supernatant was loaded on NuPAGE Novex 4-12% Bis-Tris 1.0 mm gels and subjected to electrophoresis (XCell SureLock Mini-Electrophoresis system; Invitrogen, Carlsbad, CA). Protein was transferred to a nitrocellulose membrane (iBlot Dry Blotting System; Invitrogen, Carlsbad, CA). Blocking the blot was achieved in 5% skim milk for 1 hour. The blot was then washed with 1x TBS-Tween 20 (Boston BioProducts, Ashland, MA) and incubated overnight at 4°C with 1:1000 anti-PARP1/2 in 5% skim milk (Santa Cruz Biotechnology, Santa Cruz, CA). Following three 5-minute washes and three 30-minute washes with 1x TBS-Tween 20, the blots were incubated with 1:5000 goat anti-rabbit secondary antibody at room temperature for 1hour. Then, three 5-minute washes with 1x TBS-Tween 20 were performed and blots were incubated with SuperSignal West Pico Chemiluminescent Substrate (Thermo Scientific, Rochester, NY), exposed for 20 minutes (PARP), and processed with the Kodak X-OMAT 2000A processor.

For GAPDH blots (after blocking and following three 5-minute washes with 1x TBS-Tween 20), blots were incubated for one hour at room temperature with 1:5000 anti-GAPDH in 5% skim milk (R&D Systems, Minneapolis, MN). Following three 5-minute washes with 1x TBS-Tween 20, blots were incubated with donkey anti-goat secondary antibody at room temperature for 1 hour. Following three 5-minute washes with 1x TBS-Tween 20, blots were incubated with SuperSignal West Pico Chemiluminescent Substrate for 5 minutes (Thermo Scientific, Rochester, NY), exposed for 10 seconds, and processed with the Kodak X-OMAT 2000A

processor.

2.5 *In vivo* Imaging of AZD2281-BODIPY FL and ^{18}F-AZD2281

C57BL/6J (B6) mice were obtained from the Jackson Laboratory. Nu/Nu mice (Cox-7) were obtained from Massachusetts General Hospital, Boston, MA. For all surgical procedures and imaging experiments, mice were sedated by 2.0 L/min isoflurane:2.0 L/min oxygen. For imaging experiments of more than 1 hour, the isoflurane was slowly reduced to 0.8 to 1.2 L/min. Surgeries were conducted by Rostic Gorbatov under sterile conditions with a zoom stereomicroscope (Olympus SZ61). Approval from the subcommittee on Research Animal Care at Massachusetts General Hospital was obtained for all animal protocols.

2.5.1 Tumor Xenografts

To determine *in vivo* ^{18}F-AZD2281 uptake, Nu/Nu mice each received four subcutaneous injections containing either SKOV-3, MIA PaCa2, A2780, or PANC1 cells in the flanks and shoulders (2.5×10^6 cells in 100 μL 70:30 PBS/BD matrigel per injection) (BD Biosciences, Bedford, MA). I grew all cell lines and prepared all cancerous cells for tumor injections. Either Rostic Gorbatov or I implanted tumors in all mice. Tumors were allowed to grow for two weeks before imaging.

For dose-response experiments, Nu/Nu mice each received two subcutaneous injections containing A2780 cells in the flanks (4×10^6 cells in 100 μL 70:30 PBS/BD matrigel per injection) (BD Biosciences, Bedford, MA). I grew all cell lines and prepared all cancerous cells for tumor injections. Either Greg Thurber or I performed tumor injections in all mice. Tumors were allowed to grow for two weeks before imaging.

2.5.2 Window Chambers

To determine if AZD2281-BODIPY FL accumulated in normal cells (e.g. macrophages) or tumor cells *in vivo*, HT1080 expressing H2b-apple ($1x10^6$ cells, 50 μL 1X PBS) were implanted into Dorsal Skin Chambers (DSCs, APJ Trading Co, Inc.) into the dorsal skinfold of Nu/Nu mice as described previously [46-49]. DSCs were surgically placed by Rostic Gorbatov, while implanted cells were prepared by me. To allow neovascularization, HT1080 tumors were allowed to grow for 8 days. On one side, the skin was surgically removed by Rostic Gorbatov and replaced by a 10 mm diameter optical glass cover slip held in place with a c-clip. Spacers between the both halves of the DSC frame prevent excessive compression of the tissue and vessels.

I injected mice bearing HT1080 tumors in their DSCs with 75 nmoles of AZD2281-BODIPY FL (7.5 μL DMSO, 67.5 μL, DMAC:Solutol (1:1), 150 μL 1X PBS). Immediately after injection, the accumulation and distribution of AZD2281-BODIPY FL in tumor tissue was monitored with the help of Rainer Kohler using the customized Olympus FV1000MPE based on a BX61-WI confocal microscope. Data was collected with an Olympus XLUMPLFLN 20x water immersion objective (numerical aperture/NA 1.0) and a LUMFLN (NA 1.10) water immersion objective. Excitation of AZD2281-BODIPY FL and H2b-apple was performed sequentially using a 473-nm and 599-nm diode laser, respectively, in conjunction with a DM405/488/559/635-nm dichroic beam splitter. Separation and collection of emitted light was performed with the SDM560 beam splitter and BA490-540 and BA575-675 band pass filters. Photobleaching and phototoxicity were avoided through protocol optimization using control tumors. Similar setups of lasers, splitters, and filters were used for all *in vivo* fluorescent imaging.

2.5.3 Fluorescence Imaging

Nu/Nu mice bearing A2780, PANC1, MIA PaCa2 and SKOV-3 tumors in their flanks and shoulders (n=2) were injected with either AZD2281-BODIPY FL (75 nmoles in 7.5 μL DMSO, 67.5 μL PEG400, 150 μL 1X PBS) or vehicle prepared by me and sacrificed 45 minutes post-injection. Tumors and muscle tissue from both experimental and control cohorts were excised by Thomas Reiner and Ned Keliher, and tissue fluorescence values were measured simultaneously on the Olympus OV110. Probe uptake for each tissue sample was calculated as

$$\text{Uptake} = \left. \frac{\text{mean fluorescence}}{\text{surface area}} \right|_{\substack{\text{AZD2281-} \\ \text{BODIPY FL}}} - \left. \frac{\text{mean fluorescence}}{\text{surface area}} \right|_{\text{vehicle}}$$

Equation 1. AZD2281-BODIPY FL uptake was calculated with measurements obtained on the Olympus OV110.

2.5.4 Radioactive Imaging: PET-CT

PET-CT images were acquired as reported previously in Hendricks et al., 2011.[50] All PET-CT was performed with the assistance of Jessica Truelove using a Siemens Inveon PET-CT. PET signal was calibrated before every scan by scanning an 8.0 cm phantom holding a known amount of ^{18}F isotope. Each PET acquisition lasted 45 minutes; 450 million coincidental 511 keV photon counts were registered by lutetium oxyorthosilicate crystal rings per acquisition. Photon counts were rebinned by only registering photons that bridged three or fewer consecutive rings and by applying a high resolution Fourier Rebin algorithm to reconstruct sinograms. The sinograms were then transformed into a three dimensional map of positron emission using a 2D filtered back-projection algorithm with Ramp filter at Nyquist cutoff of 0.5. Dimensions of image pixels were 0.861 mm in the x and y directions, and 0.796 mm in the z direction (total 128x128x159 pixels).

Using the Hounsfield unit scale, CT calibration was performed before acquisition with an 8.0 cm

cylindrical phantom holding water. 360 X-ray projections (cone beam angle = 9.3˚) over the 360˚ perpendicular to the animal bed were used for CT reconstruction. A 500 A anode source placed 346 mm from the center of rotation sent 80 kV X-rays to the animal bed. Projections were recorded on a CCD detector containing 2048 transaxial and 3072 axial pixels, calibrated with 70 dark and 70 light images, interpolated bilinearly, processed through a Shepp Logan filter, and reconstructed with a filtered back projection algorithm. Final isotropic CT pixel size was 110.6 m and a total of 512x512x768 pixels were recorded.

2.5.5 AZD2281-BODIPY FL and ^{18}F-AZD2281 Blood Half-lives and

Biodistribution

Thomas Reiner, Rainer Kohler, and I determined AZD2281-BODIPY FL blood half-life. Nu/Nu mice were implanted with dorsal skin chambers and injected with HT1080 cells as described in section 2.5.2. One mouse was injected with 2 nmol of AZD2281-BODIPY FL formulated in 60:40 PEG400/PBS by tail vein catheter. Light emission for three regions of interest in both vasculature and extravascular stroma was measured with the Olympus IV110. Data were recorded every ten seconds for one minute before and nine minutes after probe injection, followed by recordings every two minutes for ten minutes, and finally by recordings every 5 minutes up through 45 minutes post-injection. A final data point at 64 minutes post-injection was also recorded.

^{18}F-AZD2281 blood half-life was determined by Thomas Reiner and Ned Keliher with three C57BL/6 mice administered with 34 ± 5 μCi ^{18}F-AZD2281 by tail vein intravenous injection formulated in 5% DMSO in 1X PBS (75 μL). Blood sampling was performed by retro-orbital bleed using heparinized capillary tubes. Samples were weighed, and activity was measured by Perkin Elmer Wallac Wizard 3" 1480 Automatic Gamma counter.

Blood-half life data were fit to biexponential models in GraphPad Prism 4.0c (GraphPad Software Inc., San Diego, CA) and are calculated as the weighted averages of the distribution and clearance phases.

For biodistribution studies, six C57BL/6 mice were injected with 43 ± 5 µCi or 410 ± 22 µCi ^{18}F-AZD2281 in 5% DMSO in 1X PBS (75 µL) by tail vein intravenous injection by Thomas Reiner and Ned Keliher. Animals were sacrificed at 2 h (n = 3) or 18 h (n = 3) after injection. Tissues were excised and weighed, and activity was measured by Perkin Elmer Wallac Wizard 3" 1480 Automatic Gamma counter. GraphPad Prism 4.0c was used for statistical analysis.

2.5.6 ^{18}F-AZD2281 Imaging

All work involving handling of radioactivity was undertaken with the help of Thomas Reiner and Ned Keliher, who are both on the Weissleder lab's radioactivity research permit. To perform *in vivo* imaging of PARP1/2 expression, Nu/Nu mice bearing A2780, PANC1, MIA PaCa2 and SKOV-3 tumors (n = 3) in their left and right flanks and left and right shoulders, respectively, were injected with 500 ± 50 µCi ^{18}F-AZD2281. Ninety minutes post-injection, the mice were subjected to PET imaging. Standardized uptake values (SUVs) determined by PET imaging are defined as

$$SUV = \frac{\text{tissue radioactivity concentration}}{\text{injected radioactivity dose/body weight}}$$

Equation 2. Definition of standardized uptake value (SUV).

and were calculated following PET and CT image fusion by drawing tumor SUV margins to contain the entire tumor (guided by the aid of the CT image) using the Siemens Research Workplace v3.0 analysis application.

Mice were then sacrificed, and their tumors were excised and snap frozen in liquid nitrogen. Following decay of the radioactive tracer, I homogenized tumors in 400 µL 1x RIPA buffer and 2x Mini Complete Protease Inhibitor Cocktail tablet (Roche, Indianapolis, IN). I then performed Western blots to probe for PARP1/2 expression in the excised tumors as described above.

In order to compare PET images acquired with ^{18}F-FDG vs. ^{18}F-AZD2281 in the absence and presence of AZD2281, Nu/Nu mice bearing A2780 tumors (n = 3) in their flanks were injected with 440 ± 40 µCi ^{18}F-AZD2281 via tail vein by Thomas Reiner or Ned Keliher. Two hours post-injection, the mice were subjected to the first round of PET imaging. Thereafter, the same mice were reinjected with 523 ± 47 µCi ^{18}F-FDG and subjected to a second round of PET imaging. After ^{18}F-FDG imaging, the mice were injected with 1 mg AZD2281 formulated in 1:1:4 DMAC:Solutol: PBS (100 µL) intraperitoneally. The next day, mice were treated with 0.5 mg AZD2281 in 1:1:4 DMAC:Solutol:PBS (50 µL) intravenously. Mice were then imaged as they were on the first day. Three replicates of this treatment/imaging cycle were performed on the same mice over the following three days. A total of ten complete serial sessions were obtained for each mouse. At the conclusion of the experiment, mice were sacrificed, and their tumors were excised and activity was measured by Perkin Elmer Wallac Wizard 3" 1480 Automatic Gamma counter. SUVs were calculated following PET and CT image fusion by drawing tumor SUV margins to contain the entire tumor (guided by the aid of the CT image) using the Siemens Research Workplace v3.0 analysis application. SUV data from ^{18}F-AZD2281 PET images were decay-corrected to the start of ^{18}F-FDG PET imaging and used to correct ^{18}F-FDG SUV data.

Chapter 3: Results

3.1 *In vitro* behavior of AZD2281-derived imaging agents

3.1.1 Chemical data

Chemical structures for AZD2281, AZD2281-BODIPY FL, and ^{18}F-AZD2281 are provided in

Figure 1. Half-maximal inhibitory concentrations (IC_{50}) of AZD2281 against PARP1 and PARP2

have been reported elsewhere as 5 nM and 1 nM, respectively.[51] Using commercially available

PARP1 and PARP2 inhibition assays and statistical analysis software GraphPad Prism as

described in sections 2.1 and 2.2, I determined that the IC_{50} values for AZD2281-BODIPY FL

against PARP1 and PARP2 were 12.2 ± 1.1nM and 1.92 ± 1.2 nM, respectively (Figure 2). I also

determined that the IC_{50} value for ^{19}F-AZD2281 against PARP1 is 17.9 ± 1.1 nM (Figure 3).

3.1.2 PARP1/2 expression data

In order to obtain a qualitative estimate of relative PARP1/2 expression levels across cell lines, I

performed Western blots with protein lysate collected from harvested cell lines as described in

section 2.4.3. All cancerous cell lines exhibited increased PARP1/2 expression compared to

benign control cell line Hs832 (Figure 4).

3.1.3 Competitive inhibition using AZD2281

To determine if probe uptake occurs specifically at the molecular targets of AZD2281 (i.e.

PARP1/2), I performed AZD2281-BODIPY FL *in vitro* imaging and blocking experiments as

outlined in section 2.4.1. If AZD2281-BODIPY FL binds to PARP1/2, addition of excess

AZD2281 to cells should displace (or "block") AZD2281-BODIPY FL from the enzymes' active

sites and result in lower nuclear fluorescence intensity. Indeed, lower fluorescence at 515nm was

observed in cells treated with both AZD2281-BODIPY FL and an excess of AZD2281 (Figure

5B) than in cells treated with AZD2281-BODIPY FL alone (Figure 5A). Moreover, addition of AZD2281 displaced AZD2281-BODIPY FL from the nucleus of cells (where PARP1/2 are localized). Together, these data indicate selective uptake of AZD2281-BODIPY FL at PARP1/2. All images are adjusted with the same leveling parameters to ensure comparability of fluorescence intensities.

3.1.4 Co-localization of AZD2281-BODIPY FL with PARP1/2

To characterize and quantify the degree of AZD2281-BODIPY FL co-localization with PARP1/2 in cells, I performed immunocytochemistry with simultaneous AZD2281-BODIPY FL incubation as described in section 2.4.2 (Figure 6, Figure 7). Representative images of anti-PARP1/2 and AZD2281-BODIPY FL staining are provided in Figure 6. In all cell lines, anti-PARP1/2 and AZD2281-BODIPY FL both localized to the nucleus as defined by Hoechst 33342 staining. Fluorescence measurements were normalized to control wells to account for baseline autofluorescence of cells (515 nm; AZD2281-BODIPY FL) or for non-specific secondary antibody binding (670 nm; anti-PARP1/2). Co-localization of anti-PARP1/2 and AZD2281-BODIPY FL fluorescence signals was quantified as a Pearson's correlation coefficient comparing intensity of each pixel in the red and green channels, respectively ($R_{coloc} = 0.95$). This correlation was similar for other cancer cell lines tested (ovarian and pancreatic cancer cell lines). A summary of fluorescent signal intensities for anti-PARP1/2 (670 nm) and AZD2281-BODIPY FL (515 nm) across all cell lines investigated is provided in Figure 7. Three biological replicates and four technical replicates per biological replicate (for a total of twelve wells per cell line) were analyzed by measuring the weighted average of fluorescence intensity over at least twenty cells per well in ImageJ. Anti-PARP1/2 signal correlated with AZD2281-BODIPY FL signal across all cell lines ($R^2 = 0.858$; Figure 7B), indicating that PARP1/2 expression levels are associated with AZD2281-BODIPY FL signal strength *in vitro*.

3.2 *In vivo* behavior of AZD2281-derived imaging agents

3.2.1 Identification of cell types that accumulate AZD2281-BODIPY FL

To determine if AZD2281-BODIPY FL accumulates in cancerous cells or normal cells (e.g. macrophages) *in vivo*, Rainer Kohler and I measured probe uptake in HT1080 cells implanted into dorsal skin chambers of Nu/Nu mice as described in section 2.5.2. Co-localization (yellow) of AZD2281-BODIPY FL (green) and tumor expressed H2b-apple chromatin (red) was observed (Figure 8). Localization of AZD2281-BODIPY FL to macrophages (blue) does occur as well, but to a lower extent. This finding recapitulated the low uptake of AZD2281-BODIPY FL by leukocytes observed *in vitro* by immunocytochemistry (Figure 7) in the mouse leukemic monocyte macrophage cell line RAW 264.7. Therefore, AZD2281-BODIPY FL acts as a targeted probe for PARP1/2 *in vivo* and does not target tumors based on their increased macrophage population, which may occur for other molecular markers like Annexin Vivo (unpublished data from Sarah Earley).

3.2.2 Quantification of AZD2281-BODIPY FL uptake in xenografts

To quantify AZD2281-BODIPY FL uptake in tumor xenografts, Nu/Nu mice with four different tumors in their flanks and shoulders were injected with probe, sacrificed, and their tumors excised for imaging and Western blot as described in section 2.5.3. I prepared tumor xenografts and AZD2281-BODIPY FL injections and performed Western blots, while Thomas Reiner excised the tumors and other tissue samples from sacrificed mice. Because the skin of Nu/Nu mice fluoresces green and overlaps with the emission spectrum of AZD2281-BODIPY FL (peak 515 nm), tumors and control muscle tissue samples were removed from the mice for immediate standalone imaging (Figure 9). Tumor fluorescence intensity per unit surface area at 515 nm was higher than that of muscle tissue (Figure 9B). Furthermore, differences in fluorescence intensities

at 515nm between different tumor types reflected differences in PARP1/2 expression quantified *in vitro* by immunocytochemistry (Figure 7). A2780 cells, which had the highest level of PARP1/2 expression, had the highest relative fluorescence intensity of the four xenografted cell lines. Decreasing levels of fluorescence at 515 nm for PANC1, SKOV3, and MIA PaCa2 were observed in that order, corresponding to decreasing levels of PARP1/2 measured by *in vitro* immunocytochemistry.

3.2.3 Pharmacokinetics of ^{18}F-AZD2281

Pharmacokinetic data for AZD2281-BODIPY FL and ^{18}F-AZD2281 were measured by Thomas Reiner and Ned Keliher as described in section 2.5.5. Blood half-life of AZD2281-BODIPY FL was measured to be 6.3 minutes ($R^2 = 0.974$; Figure 10). Blood half-life of ^{18}F-AZD2281 was measured to be 12.4 minutes ($R^2 = 0.828$; Figure 11A). Biodistribution of ^{18}F-AZD2281 was evaluated at 2 hours and 18 hours post-injection by gamma counter analysis on tissue samples; ^{18}F-AZD228 undergoes hepatobiliary excretion (3.9 ± 0.9 and 3.1 ± 1.6 %ID/g for liver and small intestines, respectively, Figure 11B) and accumulates in the feces (4.3 ± 2.3 %ID/g, Figure 11C).

3.2.4 Quantification of ^{18}F-AZD2281 uptake in xenografts

To quantify ^{18}F-AZD2281 uptake in tumor xenografts, Nu/Nu mice with four different tumors in their flanks and shoulders were injected with probe, imaged with PET-CT, sacrificed, and their tumors excised for Western blot analysis as described in sections 2.5.4 and 2.5.6 (Figure 12). I prepared tumor xenografts, processed excised tumors and performed Western blots, while Thomas Reiner and Ned Keliher prepared ^{18}F-AZD2281 injections and Jessica Truelove assisted with PET-CT imaging. Standardized uptake values for ^{18}F-AZD2281 correlated with PARP1/2 expression quantified from excised tumor Western blot band densities measured with ImageJ

(R^2=0.933; Figure 12A). PET-CT images of tumors show highest levels of probe accumulation in the center of the tumor (representative images of A2780 tumor provided in Figure 12B).

3.2.5 Selective uptake of ^{18}F-AZD2281 at PARP1/2

Uptake of ^{18}F-AZD2281 and ^{18}F-FDG by tumors was compared over a series of PET-CT experiments in Nu/Nu mice bearing A2780 tumors in their flanks as described in sections 2.5.4 and 2.5.6. Baseline PET-CT images and SUVs were obtained for both ^{18}F-FDG and ^{18}F-AZD2281 on day 0 (Figure 13). Because both probes were administered to the same mice on the same day, ^{18}F signal from the first probe would not have completely decayed prior to administration of the second probe. Thus, images and SUVs for ^{18}F-AZD2281 were generated first, and signal for ^{18}F-FDG was calculated by subtracting the previously measured and decay-corrected ^{18}F-AZD2281 signal from the composite ^{18}F-AZD2281 plus ^{18}F-FDG signal. Administration of cold AZD2281 led to a significant decrease in SUVs for images generated with ^{18}F-AZD2281 but not for images of the same tumors generated with ^{18}F-FDG (P<0.001), indicating selective uptake of ^{18}F-AZD2281 at the targets of AZD2281 (i.e. PARP1/2) (Figure 13). Moreover, these data indicate that PARP1/2 inhibition can be quantified *in vivo* with ^{18}F-AZD2281.

Chapter 4: Discussion

Our results indicate that AZD2281-derived imaging probes can accurately quantify PARP1/2 expression and inhibition *in vitro* and *in vivo*. Although it was previously shown that ^{18}F-AZD2281 could image xenografts of a BRCA-mutant cell line (MDA MB436),[44] here we showed that ^{18}F-AZD2281 has expanded utility against other tumors with a range of PARP expression and that SUVs correlate with level of PARP expression. AZD2281-BODIPY FL was observed to co-localize with PARP1/2 in nuclei and nucleoli *in vitro* and accumulated in tumor cells *in vivo*. ^{18}F-AZD2281 also localized to tumor xenografts *in vivo*.

Of particular interest, PARP1/2 inhibition with AZD2281 had little effect on ^{18}F-FDG imaging, whereas ^{18}F-AZD2281 imaging produced significantly reduced signal as expected when the drug competes the probe off its target. These results suggest that while ^{18}F-FDG signal changes are unlikely to be useful in measuring PARP inhibitor uptake, ^{18}F-AZD2281 could be valuable in ongoing and future clinical trials of PARP inhibitors for direct, noninvasive quantification of drug uptake by tumors. The ability to image drug uptake could prove valuable in understanding situations where PARP inhibitor dose response differences are not significant[52] or in identifying tumors that have become resistant to PARP inhibition. ^{18}F-AZD2281 might also be useful in the prospective identification of patients with PARP-overexpressing cancers, who may benefit from treatment with PARP inhibitors. Direct quantification of PARP1/2 in patient tumors with ^{18}F-AZD2281 could help address the growing demand for tests to rapidly identify "BRCAness," a term referring to defective homologous recombination, that leads to susceptibility to PARP inhibition.[53]

Two different AZD2281-derived probes were investigated for their separate abilities to measure PARP1/2, and we found that signal from AZD2281-BODIPY FL correlated well with signal from ^{18}F-AZD2281 *in vivo* (R^2_{means}= 0.96; Figure 14). These data are compatible with the probes' shared imaging mechanism through targeted, selective uptake at PARP1/2 enzymes. Importantly, these data demonstrate that the chosen side chain modification did not greatly alter binding kinetics.

4.1 Advantages and limitations of *in vitro* measures of PARP1/2 expression

PARP1/2 expression across the panel of cell lines was evaluated by both Western blotting (Figure 4) and immunocytochemistry (Figure 7). Although Western blotting is only semi-quantitative, the most obvious limitation of Western blotting in this project was the use of multiple gels for the large number of cell lines screened. Relative amounts of PARP protein cannot be compared across gels, only within a single gel. Moreover, the metabolic enzyme GAPDH that was used as a loading control could be expressed at different levels in different cancers, though GAPDH is expressed highly at all times in most cells. For example, ten percent of total soluble skeletal muscle protein is GAPDH.[54] Choice of loading control in cancer studies is particularly challenging. Despite variations that are known to exist between cancer types in GAPDH expression,[54] the abundance of this enzyme compared to proteins of interest (i.e. PARP) still permits a rough, semi-quantitative approach to blot interpretation.

Keeping these limitations of Western blotting in mind, differences between the results obtained with blotting versus immunocytochemistry were apparent. For example, cell line A2780 appears to have moderate PARP1/2 expression by Western blot compared to the other cell lines evaluated, while A2780 had the highest PARP1/2 expression (as well as the highest level of AZD2281-BODIPY FL uptake) by immunocytochemistry. Cells used for Western blotting

versus immunocytochemistry were unavoidably subjected to slightly different stresses; for example, some of the discrepancy may be attributable to differences in cell line growth conditions, including medium pH and confluency. For Western blots, slight variances in gel composition or experimental parameters (e.g. reagents, film exposure times) could be additionally responsible for some of the divergence. Because immunocytochemistry for all cell lines was performed on 96-well plates with multiple biological and technical replicates over three independent experiments, the data obtained from the immunocytochemistry experiment is stronger and was thus used for quantification of *in vitro* PARP1/2 expression.

The limitations of applying data gained from *in vitro* experiments to *in vivo* models were also apparent; while lysates collected from cells grown *in vitro* displayed higher PARP1 than PARP2 expression by Western blot (Figure 4), cell line-derived xenografts excised from mice demonstrated higher PARP2 than PARP1 expression (Figure 9, Supplementary Figure 1). These differences are unlikely to have arisen by random error since trends of relative PARP1 and PARP2 expression were consistent across *in vitro* and *in vivo* samples. It is possible that the exposure to different sets of stresses (e.g. cell culture flasks/medium vs. subcutaneous vascularized microenvironment) led to systematic differences in gene expression. Nevertheless, because AZD2281 and its derived imaging agents bind both PARP1 and PARP2 with nanomolar affinity (Figure 2, Figure 3), and because both enzyme targets are expressed under *in vitro* and *in vivo* conditions, AZD2281-BODIPY FL and ^{18}F-AZD2281 accumulated both in cells and in xenografts.

Cell lines are laboratory tools that do not recapitulate all features of naturally arising tumors in patients. However, clinical trial data for AZD2281 suggest that PARP1/2 dependence is not

unique to certain tumor types but is a feature shared by a significant portion of human cancers, irrespective of BRCA status.[53] For example, in one study of 65 patients with ovarian carcinoma, 41% of patients with BRCA mutations and 24% of patients without BRCA mutations experienced objective responses to treatment with AZD2281.[55] Other research has confirmed that defects in tumor suppressor pathways besides BRCA (such as loss of PTEN) lead to sensitization to PARP inhibitors via synthetic lethality, suggesting upregulation of PARP in these tumors.[39] Because PARP overexpression does occur in human cancers, AZD2281-derived imaging agents can perhaps be translated to certain cohorts of patients.

4.2 Advantages and limitations of *in vivo* models of PARP1/2 imaging

Xenografts are useful tools because they are easy to set up without sacrifice of the key qualities of an *in vivo* microenvironment (e.g. vascularization, macrophage involvement). Yet, the pancreatic and ovarian cell lines evaluated in my project were after all in inappropriate anatomic locations relative to where these cancers would normally arise. Orthotopic models of these cancers are an important future step in the evaluation of AZD2281-derived imaging agents and will be especially helpful in evaluating potential signal interference from areas of high AZD2281 uptake like liver or intestines. Just as abdominal imaging with ^{18}F-FDG necessitates low blood glucose levels and can sometimes require administration of furosemide or catheterization, steps to reduce nonspecific uptake of AZD2281-derived imaging agents (such as administration of low-dose AZD2281 before imaging) may also prove necessary under certain circumstances. In contrast with conventional chemotherapy, therapeutic doses of AZD2281 produce few adverse effects[41] and a priming dose prior to imaging may be reasonable.

4.3 Future directions

In patients taking certain chemotherapeutic agents, drug-mediated DNA damage in normal tissue could upregulate PARP and increase background signal on ^{18}F-AZD2281 imaging. While we expect that this background noise would be minimal (normal cells should apoptose in the context of severe DNA damage), the effects of cytotoxic drugs on normal tissue may end up being a limiting factor for use of [8]F-AZD2281 in patients undergoing therapy with DNA-damaging drugs like cisplatin. Future experiments to evaluate ^{18}F-AZD2281 signal in mice treated with cytotoxic agents should be undertaken.

In addition to further testing of AZD2281-derived imaging agents in orthotopic and chemotherapy-treated models of cancer, experiments to evaluate uptake of ^{18}F-AZD2281 by inflamed tissue or benign lesions would be useful for determining the potential utility of the imaging agent over ^{18}F-FDG, which can be of limited utility in such situations. Also, future experiments with tumors of varying sizes could be undertaken to explore the potential for ^{18}F-AZD2281 imaging in smaller numbers of cells, as our *in vivo* xenograft model of cancer had relatively large, palpable tumors.

Over the course of our *in vivo* PET-CT experiments, we noticed that ^{18}F-FDG accumulated predominantly in the metabolically active peripheral regions of the growing tumors while ^{18}F-AZD2281 appeared to accumulate in the central regions (Figure 12,Figure 13). The differences in tropism of the probes may be due to tumor heterogeneity; while ^{18}F-FDG is known to avoid fibrotic or necrotic tissues, ^{18}F-AZD2281 may accumulate best in areas of stress (such as a hypoxic or necrotic tumor core). Histological examination of xenograft biopsies after ^{18}F-FDG

and ^{18}F-AZD2281 PET-CT imaging should be undertaken to identify any differences in cell status in areas of differential probe uptake.

Chapter 5: Conclusions

Together, these data indicate that AZD2281-based imaging agents are useful tools for *in vitro* and *in vivo* targeted visualization of PARP1/2 as well as its inhibition with emerging PARP inhibitors. As the pool of PARP inhibitors in clinical trials (summarized elsewhere)[40,56] continues to grow, non-invasive tools for quantification of PARP inhibition may become increasingly useful. Although we only imaged AZD2281-mediated inhibition of PARP in this project, PET-CT with ^{18}F-AZD2281 may indeed be able to quantify inhibition by any competitive PARP inhibitor that binds to the catalytically active site.

More broadly, this project has demonstrated the feasibility and potential applicability of using modified, targeted small molecules as imaging probes. Radiofluorination of other drugs could facilitate deeper understanding of the complicated workings of a variety of cancers as well as a number of diseases in addition to cancer. Such companion imaging agents could be readily designed and synthesized by the rapid, generic process laid out by the Weissleder group.[44,43] Patient-specific data will become increasingly vital in the management of cancers, and targeted PET-CT has the potential for meeting this need.

Summary

This project investigated the targeted molecular imaging of pancreatic and ovarian cancers with novel inhibitor-derived probes. Specifically, fluorescent and radioactive derivatives of AZD2281, a competitive PARP1/2 inhibitor currently in clinical trials for a variety of cancers, were screened in a panel of pancreatic and ovarian cancer cell lines determined to overexpress PARP1/2. We hypothesized that PARP1/2 expression and inhibition could be quantified accurately with AZD2281-derived probes.

To test this hypothesis, a panel of pancreatic ductal adenocarcinoma and ovarian carcinoma cell lines were characterized by Western blot and immunocytochemistry for PARP1/2 expression. AZD2281-derived probes were observed to co-localize with PARP1/2 in the nucleus and especially in the nucleoli of all cell lines examined *in vitro*. Accumulation of AZD2281-BODIPY FL correlated with PARP1/2 expression, with the highest PARP1/2 expressers accruing the most AZD2281-BODIPY FL, indicating that PARP1/2 expression is a determinant of fluorescent signal strength of AZD2281-BODIPY FL *in vitro*.

To determine the utility of AZD2281-derived probes *in vivo*, four cell lines representing a range of PARP1/2 expression levels were xenografted into Nu/Nu mice. Mice bearing four tumor types each were imaged with AZD2281-BODIPY FL or ^{18}F-AZD2281, sacrificed, and their tumors excised for stand-alone imaging and Western blot. Tumor fluorescence and SUVs from PET-CT correlated with tumor PARP1/2 expression determined by Western blot, indicating that PARP1/2 expression level is a determinant of fluorescent and radioactive signal strength *in vivo*. Significantly more AZD2281-derived probe accumulated in tumors than in control muscle tissue,

indicating that both probes are useful for detecting PARP1/2-overexpressing cells amongst background normal tissue *in vivo*.

We also compared our radioactive derivative ^{18}F-AZD2281 with the current standard radiotracer of PET imaging, ^{18}F-FDG. A2780 cells, which were determined to highly express PARP1/2, were implanted into the flanks of a cohort of mice and allowed to grow. These mice were imaged before and after receiving doses of unmodified AZD2281 drug in triplicate. While SUVs for ^{18}F-FDG were unchanged by the administration of AZD2281, ^{18}F-AZD2281 SUVs significantly decreased compared to baseline signal, in keeping with the ability of similarly structured molecules to compete at their target enzyme. These data indicate that ^{18}F-AZD2281 may find use in quantifying PARP1/2 inhibition noninvasively.

Because it binds to the active site of PARP1/2, ^{18}F-AZD2281 could be used to noninvasively quantify inhibition by other competitive PARP inhibitors, though we only investigated AZD2281 inhibition in this project. We also believe ^{18}F-AZD2281 could be useful for prospective identification of patients with cancers that may be susceptible to treatment with PARP inhibitors.

More generally, the modification of targeted small molecules may enable noninvasive studies of other enzyme targets in patients with a variety of diseases. Using targeted radiotracers in PET-CT imaging has the potential to meet the growing demand for rapid methods of ascertaining patient-specific cancer properties, such as susceptibility to treatment, early identification of resistance, and recurrence.

References

1. Pittet, M. J. & Weissleder, R. Intravital imaging. *Cell* **147**, 983-991 (2011).
2. Weissleder, R. & Pittet, M. J. Imaging in the era of molecular oncology. *Nature* **452**, 580-589 (2008).
3. National Cancer Institute. SEER Stat Fact Sheets: Ovary. (2013).
4. Ushijima, K. Treatment of Recurrent Ovarian Cancer - At First Relapse. *J Oncol.* **2010**, 497429 (2010).
5. Rutherford, T. et al. A prospective study evaluating the clinical relevance of a chemoresponse assay for treatment of patients with persistent or recurrent ovarian cancer. *Gynecologic Oncology* **131**, 362-367 (2013).
6. National Cancer Institute. SEER Stat Fact Sheets: Pancreas. (2013).
7. Sangar, V. et al. Use of pharmacogenomic modeling in pancreatic cancer for prediction of chemotherapy response and resistance. *2013 Gastrointestinal Cancers Symposium* Abstract 142 (2013).
8. National Cancer Institute. PDQ Pancreatic Cancer Treatment. (2013).
9. Nanni, C. et al. (18)F-FDG PET/CT in the evaluation of recurrent ovarian cancer: a prospective study on forty-one patients. *Eur J Surg Oncol* **31**, 792-797 (2005).
10. Avril, N. et al. Prediction of response to neoadjuvant chemotherapy by sequential F-18-fluorodeoxyglucose positron emission tomography in patients with advanced-stage ovarian cancer. *J Clin Oncol* **23**, 7445-7453 (2005).
11. Picchio, M. et al. Advanced ovarian carcinoma: usefulness of [(18)F]FDG-PET in combination with CT for lesion detection after primary treatment. *Q J Nucl Med* **47**, 77-84 (2003).
12. Lonsdale, M. N. & Beyer, T. Dual-modality PET/CT instrumentation-today and tomorrow. *Eur J Radiol* **73**, 452-460 (2010).
13. Ben-Haim, S. & Ell, P. 18F-FDG PET and PET/CT in the evaluation of cancer treatment response. *J Nucl Med* **50**, 88-99 (2009).
14. Grassetto, G. et al. FDG PET/CT in Ovarian Cancer: What About Treatment Response and Prognosis? *Clin Nucl Med* **37**, 54-56 (2012).
15. Zimny, M. et al. Fluorine-18 fluorodeoxyglucose positron emission tomography in the differential diagnosis of pancreatic carcinoma: a report of 106 cases. *Eur J Nucl Med* **24**, 678-682 (1997).
16. Wadsak, W. & Mitterhauser, M. Basics and principles of radiopharmaceuticals for PET/CT. *Eur J Radiol* **73**, 461-469 (2010).
17. Boellaard, R. et al. FDG PET and PET/CT: EANM procedure guidelines for tumour PET imaging: version 1.0. *Eur J Nucl Med Mol Imaging* **37**, 181-200 (2010).
18. Vallabhajosula, S. (18)F-labeled positron emission tomographic radiopharmaceuticals in oncology: an overview of radiochemistry and mechanisms of tumor localization. *Semin Nucl Med* **37**, 400-419 (2007).
19. Basu, S. et al. Fundamentals of PET and PET/CT imaging. *Ann N Y Acad Sci* **1228**, 1-18 (2011).

20. Blake, G. M., Park-Holohan, S. J., Cook, G. J. & Fogelman, I. Quantitative studies of bone with the use of 18F-fluoride and 99mTc-methylene diphosphonate. *Semin Nucl Med* **31**, 28-49 (2001).
21. Cornell, R., Grove, G. L., Rothblat, G. H. & Horwitz, A. F. Lipid requirement for cell cycling. The effect of selective inhibition of lipid synthesis. *Exp Cell Res* **109**, 299-307 (1977).
22. Salskov, A., Tammisetti, V. S., Grierson, J. & Vesselle, H. FLT: measuring tumor cell proliferation in vivo with positron emission tomography and 3'-deoxy-3'-[18F]fluorothymidine. *Semin Nucl Med* **37**, 429-439 (2007).
23. Whitmore, G. F. & Varghese, A. J. The biological properties of reduced nitroheterocyclics and possible underlying biochemical mechanisms. *Biochem Pharmacol* **35**, 97-103 (1986).
24. Rice, S. L., Roney, C. A., Daumar, P. & Lewis, J. S. The next generation of positron emission tomography radiopharmaceuticals in oncology. *Semin Nucl Med* **41**, 265-282 (2011).
25. Van de Wiele, C., De Vos, F., Slegers, G., Van Belle, S. & Dierckx, R. A. Radiolabeled estradiol derivatives to predict response to hormonal treatment in breast cancer: a review. *Eur J Nucl Med* **27**, 1421-1433 (2000).
26. Kiesewetter, D. O. et al. Preparation of four fluorine- 18-labeled estrogens and their selective uptakes in target tissues of immature rats. *J Nucl Med* **25**, 1212-1221 (1984).
27. Divgi, C. R. et al. Preoperative characterisation of clear-cell renal carcinoma using iodine-124-labelled antibody chimeric G250 (124I-cG250) and PET in patients with renal masses: a phase I trial. *Lancet Oncol* **8**, 304-310 (2007).
28. Hilton, J. L. et al. Inactivation of BRCA1 and BRCA2 in ovarian cancer. *J Natl Cancer Inst* **94**, 1396-1406 (2002).
29. Ottenhof, N. A., de Wilde, R. F., Maitra, A., Hruban, R. H. & Offerhaus, G. J. Molecular characteristics of pancreatic ductal adenocarcinoma. *Patholog Res Int* **2011**, 620601 (2011).
30. Gudmundsdottir, K. & Ashworth, A. The roles of BRCA1 and BRCA2 and associated proteins in the maintenance of genomic stability. *Oncogene* **25**, 5864-5874 (2006).
31. Farmer, H. et al. Targeting the DNA repair defect in BRCA mutant cells as a therapeutic strategy. *Nature* **434**, 917-921 (2005).
32. Bryant, H. E. et al. Specific killing of BRCA2-deficient tumours with inhibitors of poly(ADP-ribose) polymerase. *Nature* **434**, 913-917 (2005).
33. Evers, B. et al. Selective inhibition of BRCA2-deficient mammary tumor cell growth by AZD2281 and cisplatin. *Clin Cancer Res* **14**, 3916-3925 (2008).
34. Rouleau, M., Patel, A., Hendzel, M. J., Kaufmann, S. H. & Poirier, G. G. PARP inhibition: PARP1 and beyond. *Nat Rev Cancer* **10**, 293-301 (2010).
35. Ashworth, A. A synthetic lethal therapeutic approach: poly(ADP) ribose polymerase inhibitors for the treatment of cancers deficient in DNA double-strand break repair. *J Clin Oncol* **26**, 3785-3790 (2008).
36. Ame, J. C. et al. PARP-2, A novel mammalian DNA damage-dependent poly(ADP-ribose) polymerase. *J Biol Chem* **274**, 17860-17868 (1999).
37. El-Khamisy, S. F., Masutani, M., Suzuki, H. & Caldecott, K. W. A requirement for PARP-1 for the assembly or stability of XRCC1 nuclear foci at sites of oxidative DNA damage. *Nucleic Acids Res* **31**, 5526-5533 (2003).
38. McCabe, N. et al. Deficiency in the repair of DNA damage by homologous recombination and sensitivity to poly(ADP-ribose) polymerase inhibition. *Cancer Res* **66**, 8109-8115 (2006).

39. Mendes-Pereira, A. M. et al. Synthetic lethal targeting of PTEN mutant cells with PARP inhibitors. *EMBO Mol Med* **1**, 315-322 (2009).
40. Ferraris, D. V. Evolution of poly(ADP-ribose) polymerase-1 (PARP-1) inhibitors. From concept to clinic. *J Med Chem* **53**, 4561-4584 (2010).
41. Fong, P. C. et al. Inhibition of poly(ADP-ribose) polymerase in tumors from BRCA mutation carriers. *N Engl J Med* **361**, 123-134 (2009).
42. Keliher, E. J., Reiner, T., Turetsky, A., Hilderbrand, S. A. & Weissleder, R. High-yielding, two-step 18F labeling strategy for 18F-PARP1 inhibitors. *ChemMedChem* **6**, 424-427 (2011).
43. Reiner, T., Earley, S., Turetsky, A. & Weissleder, R. Bioorthogonal small-molecule ligands for PARP1 imaging in living cells. *Chembiochem* **11**, 2374-2377 (2010).
44. Reiner, T., Keliher, E. J., Earley, S., Marinelli, B. & Weissleder, R. Synthesis and in vivo imaging of a 18F-labeled PARP1 inhibitor using a chemically orthogonal scavenger-assisted high-performance method. *Angew Chem Int Ed Engl* **50**, 1922-1925 (2011).
45. Reiner, T. et al. Imaging Therapeutic PARP Inhibition *In Vivo* through Bioorthogonally Developed Companion Imaging Agents. *Neoplasia* **14**, 169-177 (2012).
46. Falkvoll, K. H., Rofstad, E. K., Brustad, T. & Marton, P. A transparent chamber for the dorsal skin fold of athymic mice. *Exp Cell Biol* **52**, 260-268 (1984).
47. Orth, J. D. et al. Analysis of mitosis and antimitotic drug responses in tumors by in vivo microscopy and single-cell pharmacodynamics. *Cancer Res* **71**, 4608-4616 (2011).
48. Lehr, H. A., Leunig, M., Menger, M. D., Nolte, D. & Messmer, K. Dorsal skinfold chamber technique for intravital microscopy in nude mice. *Am J Pathol* **143**, 1055-1062 (1993).
49. Makale, M. Intravital imaging and cell invasion. *Methods Enzymol* **426**, 375-401 (2007).
50. Hendricks, J. A. et al. In vivo PET imaging of histone deacetylases by 18F-suberoylanilide hydroxamic acid (18F-SAHA). *J Med Chem* **54**, 5576-5582 (2011).
51. Menear, K. A. et al. 4-[3-(4-cyclopropanecarbonylpiperazine-1-carbonyl)-4-fluorobenzyl]-2H-phth alazin-1-one: a novel bioavailable inhibitor of poly(ADP-ribose) polymerase-1. *J Med Chem* **51**, 6581-6591 (2008).
52. Kaye, S. B. et al. Phase II, Open-Label, Randomized, Multicenter Study Comparing the Efficacy and Safety of Olaparib, a Poly (ADP-Ribose) Polymerase Inhibitor, and Pegylated Liposomal Doxorubicin in Patients With BRCA1 or BRCA2 Mutations and Recurrent Ovarian Cancer. *J Clin Oncol* (2011).
53. Sessa, C. Update on PARP1 inhibitors in ovarian cancer. *Ann Oncol* **22 Suppl 8**, viii72-viii76 (2011).
54. Seidler, N. W. in *GAPDH: Biological Properties and Diversity* 1-36 (Springer, New York, 2013).
55. Gelmon, K. A. et al. Olaparib in patients with recurrent high-grade serous or poorly differentiated ovarian carcinoma or triple-negative breast cancer: a phase 2, multicentre, open-label, non-randomised study. *Lancet Oncol* **12**, 852-861 (2011).
56. Yuan, Y., Liao, Y. M., Hsueh, C. T. & Mirshahidi, H. R. Novel targeted therapeutics: inhibitors of MDM2, ALK and PARP. *J Hematol Oncol* **4**, 16 (2011).

Tables

Table 1. Factors Leading to Increased or Decreased ^{18}F-FDG Uptake in Tumors

	Increased 18F-FDG uptake	Decreased 18F-FDG uptake
Viable cancer cell number	✕	
Tumor perfusion	✕	
Hypoxia	✕	
Glucose transporter expression	✕	
Hexokinase activity	✕	
Inflammation or infection	✕	
Receptor antagonists	✕	
Chemotherapy (acute)	✕	
Radiation therapy (acute)	✕	
Receptor blockade		✕
Chemotherapy (effective)		✕
Radiation therapy (chronic)		✕
Hyperglycemia		✕
Insulin		✕
Necrosis		✕

Modified from Vallabhajosula et al.[18]

Figures

A)

B)

C)
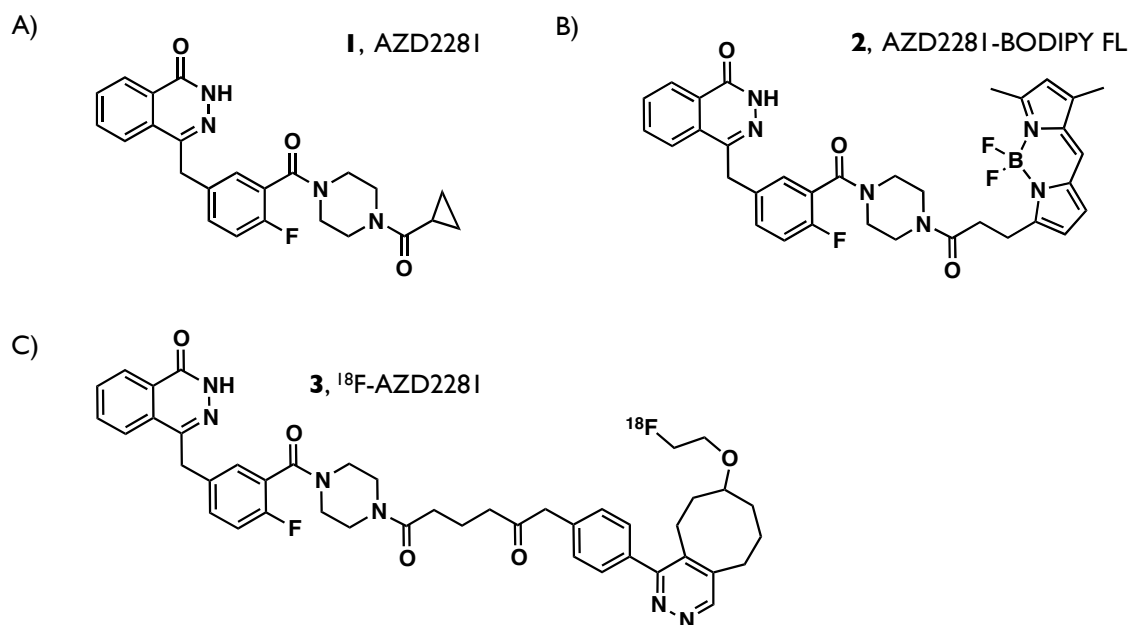
Figure 1. Chemical structures of A) AZD2281 (Olaparib; Selleck Chemicals, Houston, TX), B) AZD2281-BODIPY FL, and C) ^{18}F-AZD2281. (Reiner and Lacy et al 2012)[45]

A)

IC50 of AZD2281-BODIPY FL

B)

PARP2

$IC_{50, PARP1} = 12.2 \pm 1.1 nM$

$IC_{50, PARP2} = 1.92 \pm 1.2 nM$
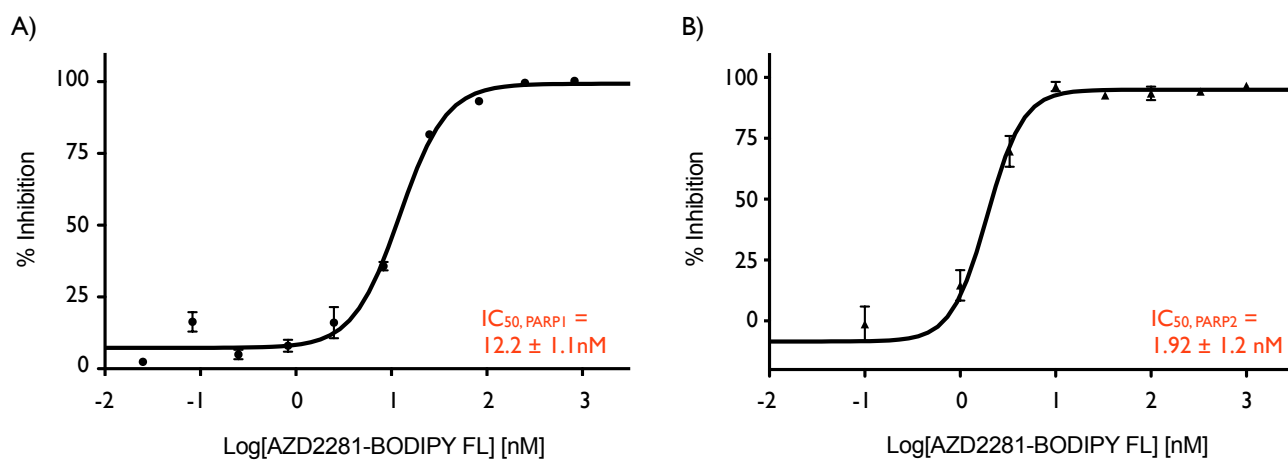
Figure 2. IC_{50} of AZD2281-BODIPY FL measured for A) PARP1 with the Universal PARP1 Colorimetric Assay Kit (Trevigen; 4677-096-K) and for B) PARP2 with the PARP2 Chemiluminescent Assay Kit (BPS Biosciences; 80552).
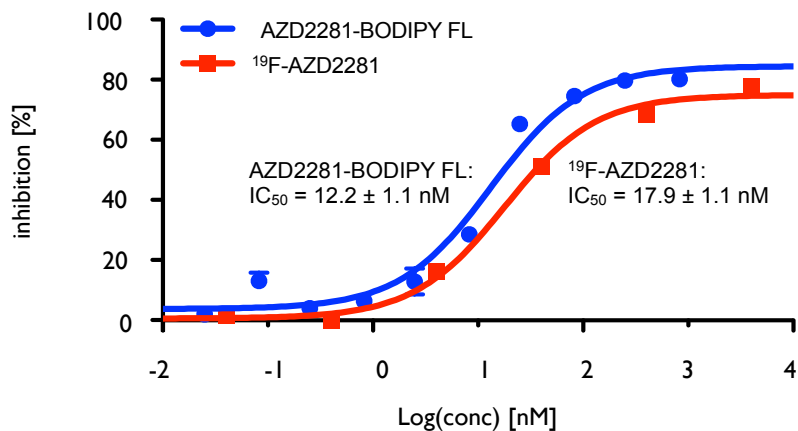
Figure 3. IC_{50} curves for AZD2281-BODIPY FL (blue) and ^{19}F-AZD2281 (red) measured for PARP1 with the Universal PARP1 Colorimetric Assay Kit (Trevigen; 4677-096-K). (Reiner and Lacy et al 2012)[45]
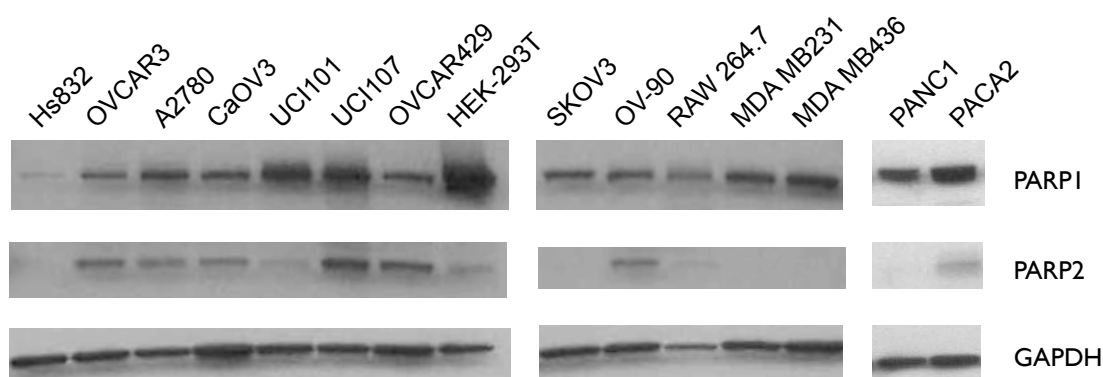
Figure 4. PARP1 expression in cell lines derived from human ovarian papillary serous adenocarcinomas (UCI101, UCI107, A2780, OVCAR3, CaOV3, SKOV3, OV-90), ovarian serous cystoadenocarcinoma (OVCAR429), pancreatic ductal adenocarcinomas (Panc1, Paca2), and mammary adenocarcinoma (MDA MB231, MDA MB436). Benign ovarian cyst Hs832 (noncancerous control), mouse leukemic monocyte macrophage RAW 264.7, and human embryonic kidney cell line 293T (positive control) are also included for comparison. Anti-PARP1/2 Rab (Santa Cruz Biotechnology; SC-7150), anti-GAPDH Gab (R&D Systems; AF5718).
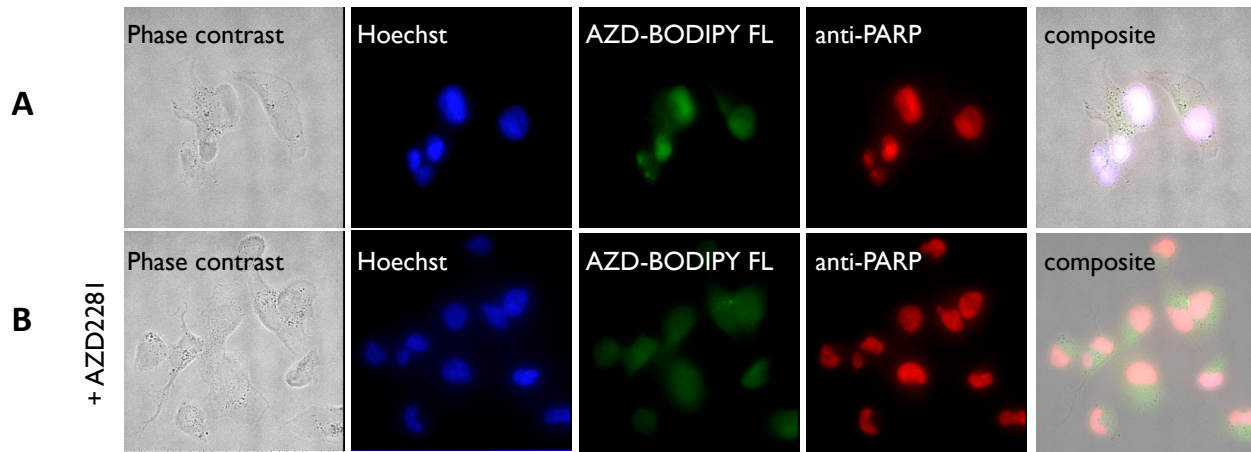
Figure 5. Cells were seeded on 8-well chamber slides and allowed to attach overnight. AZD2281-BODIPY FL (1 μM) (A) or AZD2281-BODIPY FL (1 μM) + AZD2281 (100 μM) (B) was added to live cells and incubated for 20 minutes. Cells were then fixed, stained with anti-PARP antibody (Millipore; MAB3290), mounted, and imaged with Nikon 80i (60x, 1x zoom). A) MDA MB231, B) MDA MB231 blocked with cold AZD2281. Images are representative of AZD2281-BODIPY FL behavior observed in all cell lines investigated with blocking expeirments.
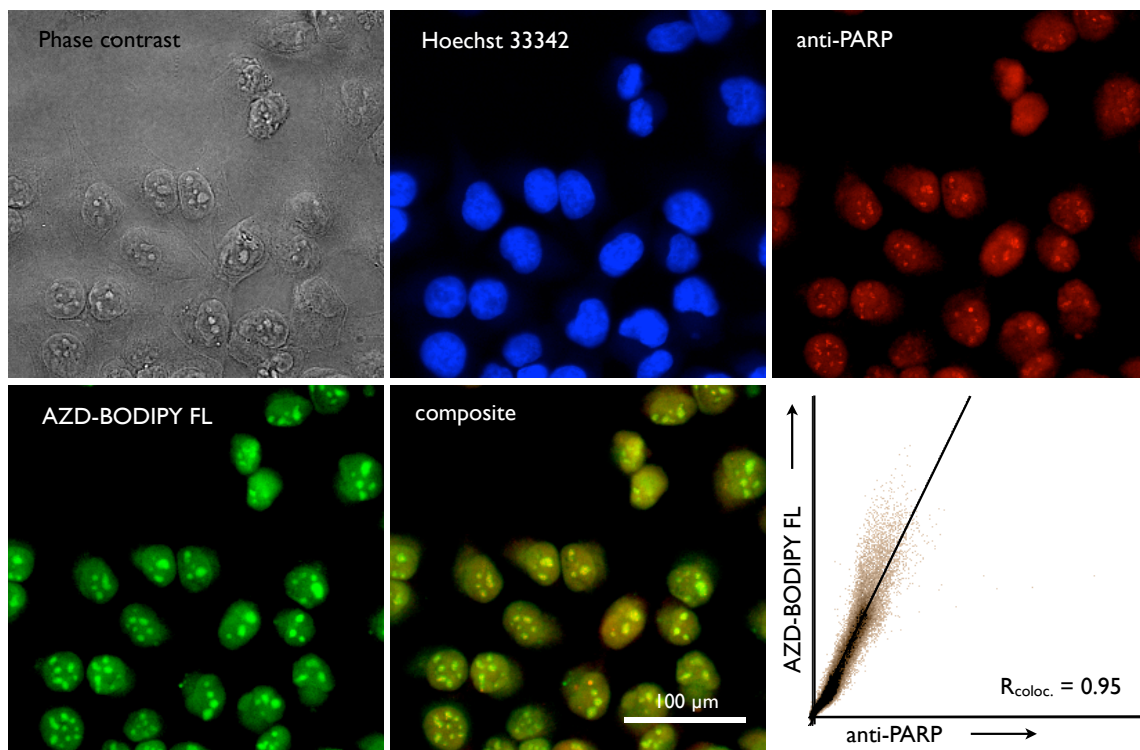
Figure 6. PANC1 cells were seeded on 96-well plates and allowed to attach overnight. AZD2281-BODIPY FL (1 μM) was added to live cells and incubated for 20 minutes. Cells were then fixed, stained with anti-PARP1/2 antibody (Santa Cruz Biotechnology; SC-7150), mounted, and imaged with the Deltavision microscopy system on the Olympus IX71. Co-localization was assessed with ImageJ. (Reiner and Lacy et al 2012)[45]
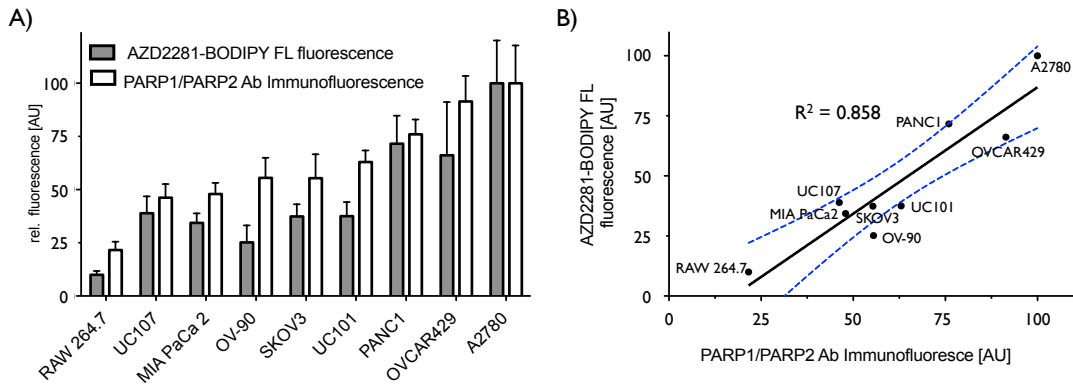
Figure 7. Cells were seeded at a density of 5,000 cells per well in 96-well plates and were grown for 48 hours. AZD2281-BODIPY FL (1 µM) was added to live cells and incubated for 20 minutes. Cells were then fixed, stained with anti-PARP1/2 antibody (Santa Cruz Biotechnology; SC-7150), mounted, and imaged with the Deltavision/Olympus IX71 microscopy system. Fluorescence intensities were measured with ImageJ. A. Fluorescence intensities for AZD2281-BODIPY FL and anti-PARP1/2 are plotted for each cell line. B. Mean AZD2281-BODIPY fluorescence intensity plotted against mean anti-PARP1/2 fluorescence intensity, with 95% confidence band shown by dotted blue curves. Twelve replicate wells with at least 20 cellular fluorescence measurements per well were used for each cell line. (Reiner and Lacy et al 2012)[45]
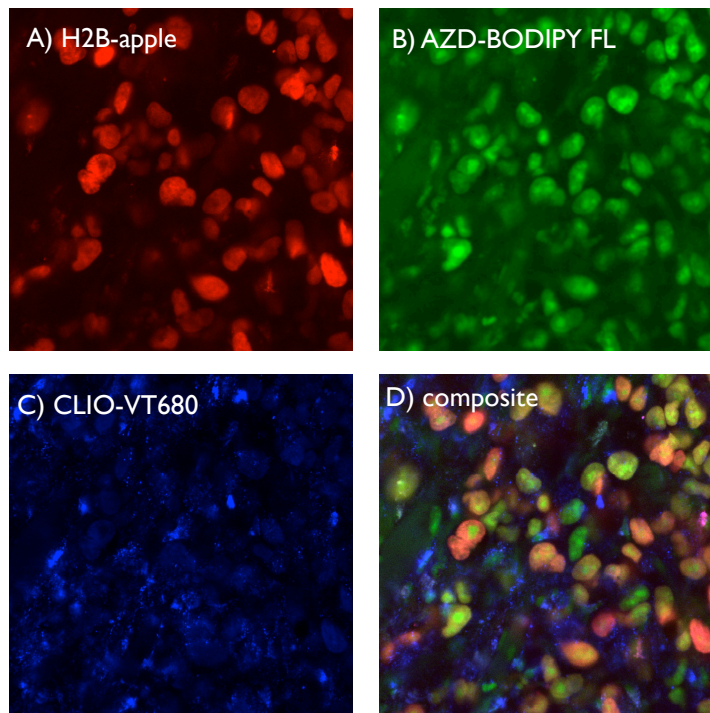
Figure 8. HT180 cells stably expressing H2b-apple, which labels chromatin, were implanted into dorsal skin chambers of Nu/Nu mice and allowed to vascularize over 8 days. Mice were then injected with 75 nmoles of AZD2281-BODIPY FL and imaged with the Olympus FV1000MPE. A composite image (D) shows co-localization (yellow) of tumor expressed H2b-apple chromatin (A; red) and AZD2281-BODIPY FL (B; green). AZD2281-BODIPY FL does not co-localize with CLIO-VivoTag680, which labels leukocytes (C; blue).
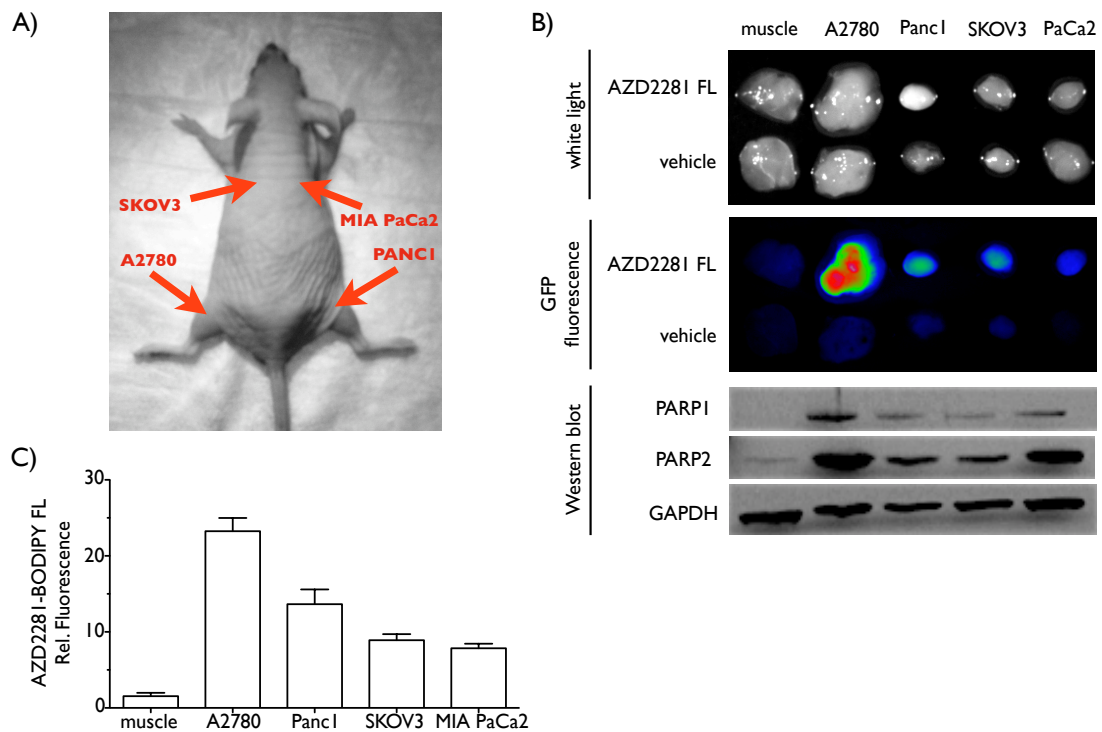
Figure 9. Nu/Nu mice bearing A2780, PANC1, MIA PaCa2 and SKOV3 tumors in their flanks and shoulders were injected with either AZD2281-BODIPY FL (75 nmoles in 7.5 μL DMSO, 67.5 μL PEG400, 150 μL 1X PBS) or vehicle and sacrificed 45 minutes post-injection. Tumors and muscle tissue from both experimental and control cohorts were excised and their fluorescence was measured on the Olympus OV110. A). Arrangement of tumor sites to be xenografted onto an isoflurane anesthetized Nu/Nu mouse. B). Visible light and fluorescence images of the excised tissues from both AZD2281-BODIPY FL-injected and vehicle-injected mice. Western blot of excised tumor lysate showing PARP1 and PARP2 expression is also shown. C). Relative fluorescence intensities of the excised tissues normalized to vehicle-only fluorescence level.
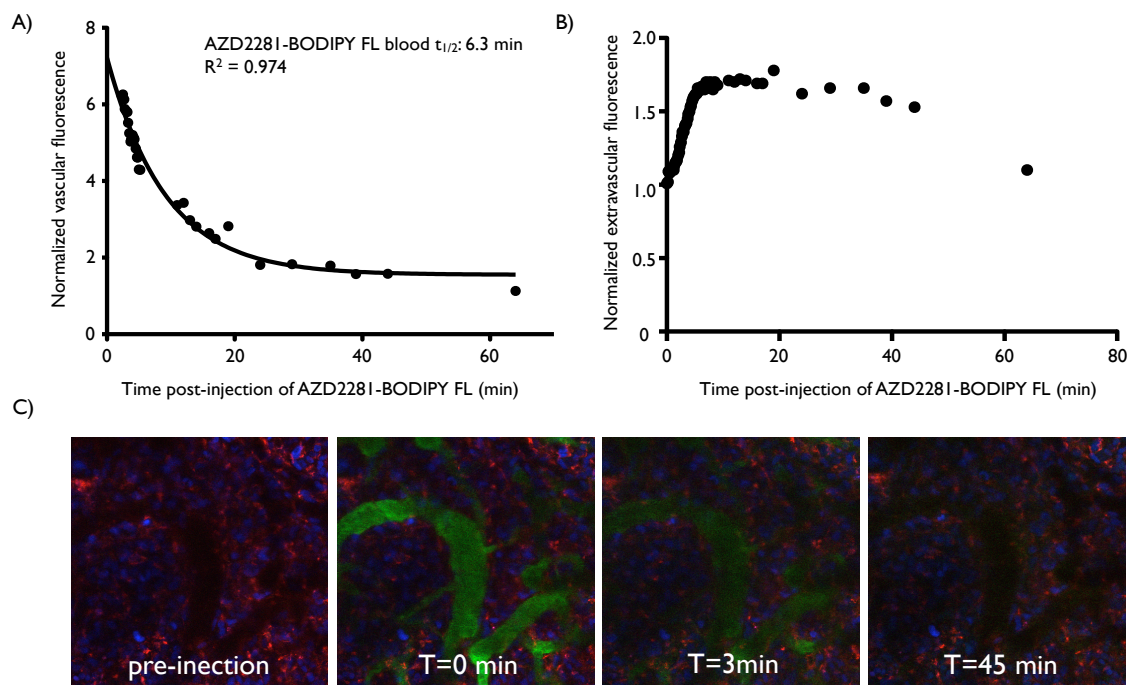
Figure 10. One Nu/Nu mouse bearing A2780, PANC1, MIA PaCa2, and SKOV3 tumors in its shoulders and flanks was imaged on the Olympus FV1000MPE over the course of 60 minutes to calculate AZD2281-BODIPY FL blood half-life. A). Vascular fluorescence over time, normalized to vascular fluorescence before AZD2281-BODIPY FL injection. B). Extravascular fluorescence over time, normalized to extravascular fluorescence before AZD2281-BODIPY FL injection. C). Representative images at indicated time points pre- and post- probe injection of a particular blood vessel in the field of the DSC. AZD2281-BODIPY FL is represented in green, HT1080 H2b-apple expressing cells are in blue, and macrophages are in red.
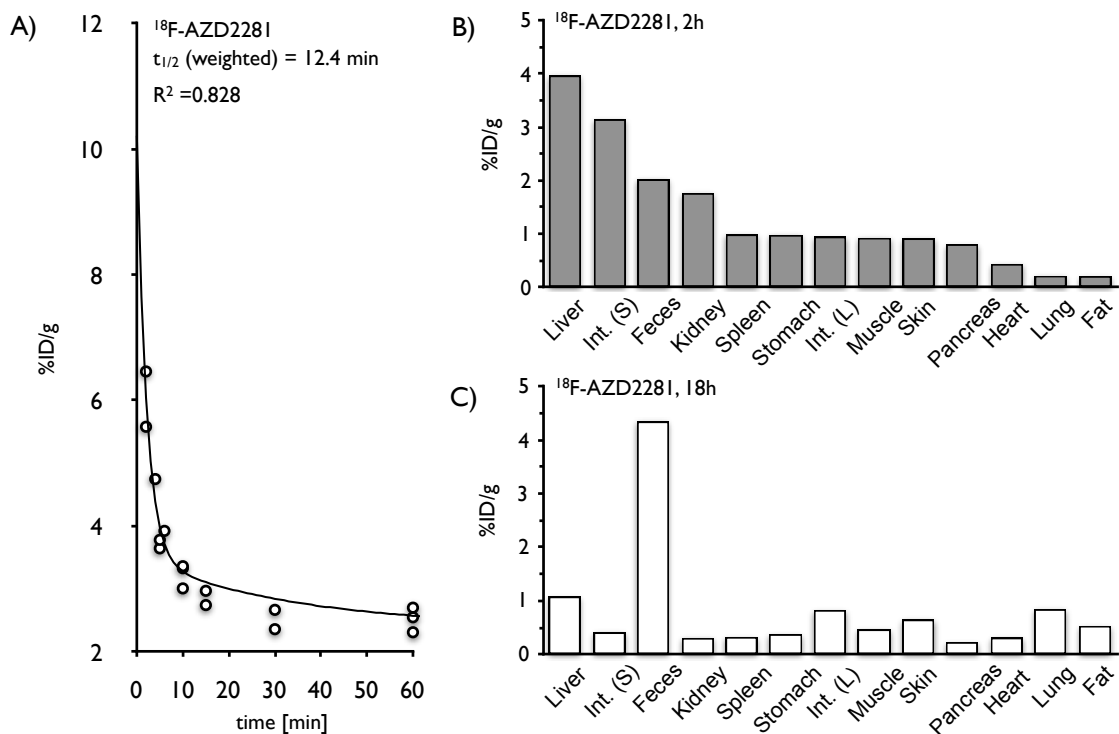
Figure 11. Blood half-life and biodistribution of ^{18}F-AZD2281. A). Blood half-life was determined with three C57BL/6 mice administered with 100 ± 25 μCi ^{18}F-AZD2281 by tail vein intravenous injection formulated in 70% 1X PBS, 10% DMSO in water, 20% DMAC:Solutol (1:1). Blood sampling was performed by retro-orbital bleed using tared capillary tubes. Samples were weighed, and activity was measured by γ counter. B) & C). Six C57BL/6 mice were injected with 100 ± 25 μCi or 600 ± 50 μCi ^{18}F-AZD2281 by tail vein iv injection. Animals were sacrificed at B) 2 h (n = 3) or C) 18 h (n = 3) after injection. Tissues were excised and weighed, and activity was measured by γ counter. (Reiner and Lacy et al 2012)[45]
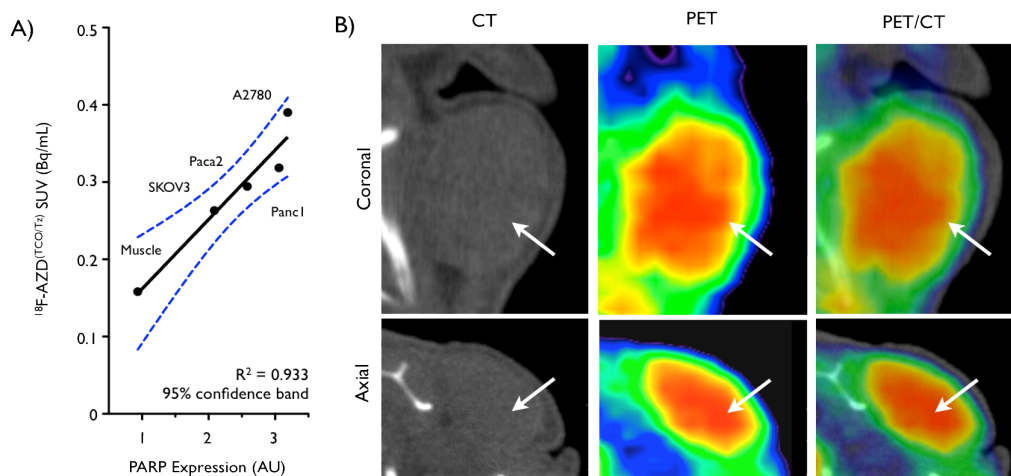

Figure 12. In vivo imaging of PARP. Nu/Nu mice bearing A2780, Panc1, MIA PaCa2 and SKOV3 tumors (n = 3) in their flanks and shoulders were injected with 500 ± 50 μCi ^{18}F-AZD2281. Ninety minutes post-injection, the mice were subjected to PET imaging. A). Standardized uptake values (SUVs) determined by PET imaging correlated with PARP1/2 expression determined by Western blot of excised tumor lysate. B). Representative coronal (top) and axial (bottom) CT, PET, and PET/CT slices for an A2780 tumor. (Reiner and Lacy et al 2012)[45]
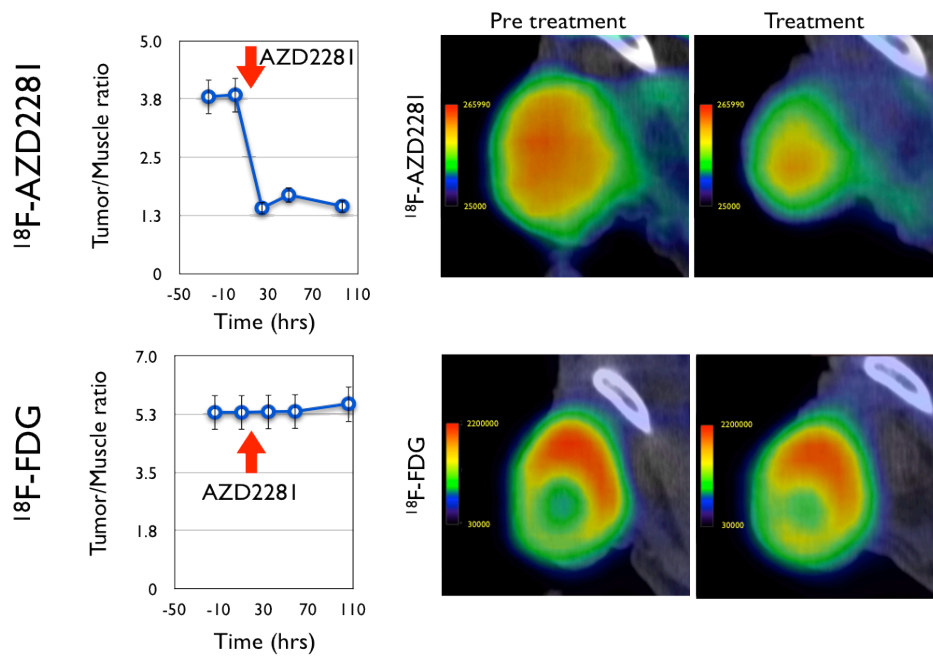
Figure 13. Nu/Nu mice bearing A2780 tumors (n = 3) in their flanks were injected with 440 ± 40 μCi ^{18}F-AZD2281 and PET imaged 2 hours later. Thereafter, the same mice were intravenously injected with 523 ± 47 μCi ^{18}F-FDG and subjected to a second round of PET imaging. After ^{18}F-FDG imaging, the mice were injected with 1 mg AZD2281 intraperitoneally. The next day, mice were treated with 0.5 mg AZD2281 intravenously. Mice were then imaged as they had been on the first day. Three replicates of this treatment/imaging protocol were performed on the same mice over three days. A total of ten complete serial sessions were acquired for each mouse. Tumor SUV margins were drawn to span the entire tumor using the Siemens Research Workplace v3.0 analysis application. SUV data from ^{18}F-AZD2281 PET images were decay corrected to the start of ^{18}F-FDG PET imaging and used to correct ^{18}F-FDG SUV data. (Reiner and Lacy et al 2012)[45]
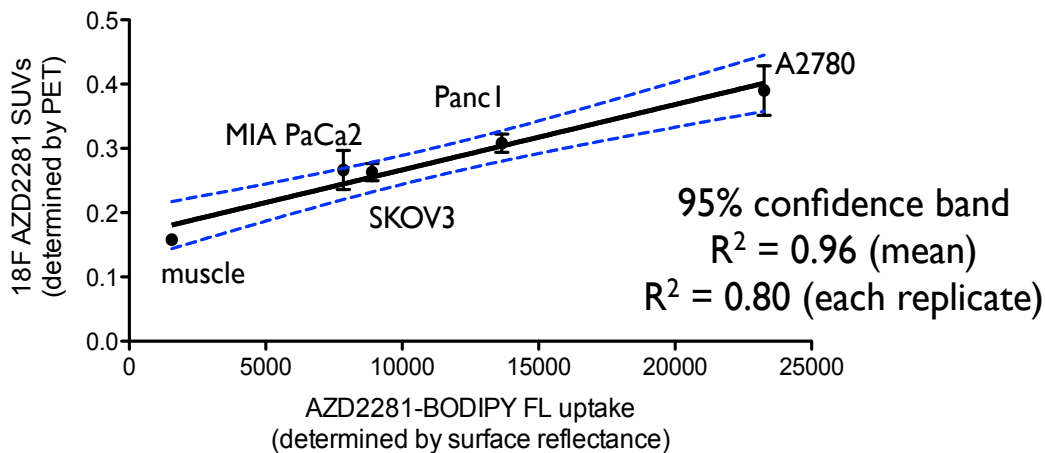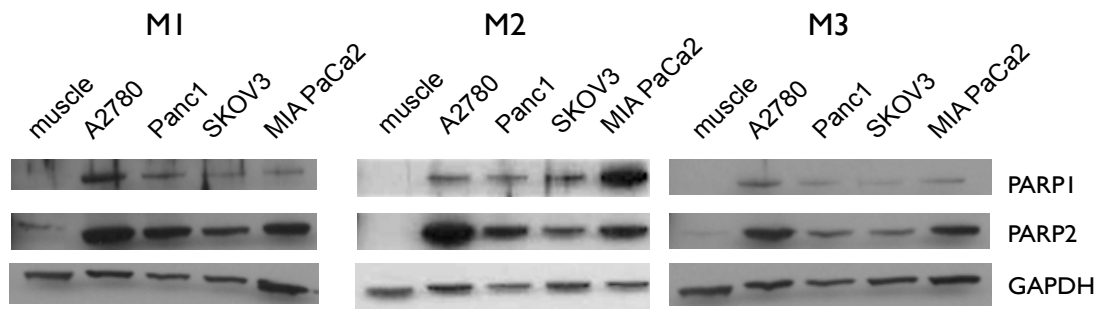

Figure 14. *In vivo* comparison of signals measured in tumor xenografts from ^{18}F-AZD2281 (SUVs) and AZD2281-BODIPY FL (surface reflectance; arbitrary units). Nu/Nu mice bearing A2780, Panc1, MIA PaCa2 and SKOV3 tumors in their flanks and shoulders were used for PET-CT and fluorescence imaging. (Reiner and Lacy et al 2012)[45]

Supplementary Figures

Supplementary Figure 1. PARP1 and PARP2 expression evaluated by Western blot for excised tumors from three Nu/Nu mice bearing four tumors (A2780, Panc1, SKOV3, MIA PaCa2) each in their flanks and shoulders. Anti-PARP1/2 Rab (Santa Cruz Biotechnology; SC-7150), anti-GAPDH Gab (R&D Systems; AF5718).